THE EFFECT OF STRAIN RATE AND TEMPERATURE ON DEEP DRAWING FOR DIFFERENT CONSTITUTIVE RELATIONS

A THESIS SUBMITTED TO
THE GRADUATE SCHOOL OF NATURAL AND APPLIED SCIENCES
OF
MIDDLE EAST TECHNICAL UNIVERSITY

BY

SEÇKİN GÖKŞEN

IN PARTIAL FULFILLMENT OF THE REQUIREMENTS
FOR
THE DEGREE OF MASTER OF SCIENCE
IN
MECHANICAL ENGINEERING

AUGUST 2019

Approval of the thesis:

THE EFFECT OF STRAIN RATE AND TEMPERATURE ON DEEP DRAWING FOR DIFFERENT CONSTITUTIVE RELATIONS

submitted by **SEÇKİN GÖKŞEN** in partial fulfillment of the requirements for the degree of **Master of Science in Mechanical Engineering Department, Middle East Technical University** by,

Prof. Dr. Halil Kalıpçılar
Dean, Graduate School of **Natural and Applied Sciences** _____

Prof. Dr. M. A. Sahir Arıkan
Head of Department, **Mechanical Engineering** _____

Prof. Dr. Haluk Darendeliler
Supervisor, **Mechanical Engineering, METU** _____

Examining Committee Members:

Prof. Dr. Süha Oral
Mechanical Engineering Dept., METU _____

Prof. Dr. Haluk Darendeliler
Mechanical Engineering, METU _____

Prof. Dr. Suat Kadıoğlu
Mechanical Engineering Dept., METU _____

Assist. Prof. Dr. Orkun Özşahin
Mechanical Engineering Dept., METU _____

Prof. Dr. Can Çoğun
Mechatronics Engineering Dept., Cankaya University _____

Date: 06.08.2019

I hereby declare that all information in this document has been obtained and presented in accordance with academic rules and ethical conduct. I also declare that, as required by these rules and conduct, I have fully cited and referenced all material and results that are not original to this work.

Name, Surname: Seçkin Gökşen

Signature:

ABSTRACT

THE EFFECT OF STRAIN RATE AND TEMPERATURE ON DEEP DRAWING FOR DIFFERENT CONSTITUTIVE RELATIONS

Gökşen, Seçkin
Master of Science, Mechanical Engineering
Supervisor: Prof. Dr. Haluk Darendeliler

August 2019, 105 pages

In this study, the effects of strain rate and temperature on deep drawing process are investigated by considering different yield criteria and hardening models. For this purpose, various punch velocity and temperature values are considered using 1 mm-thick DKP6112 and AZ31 sheet materials. The results are compared according to thickness strain distribution and punch force obtained by a commercial finite element software. To express constitutive relations of corresponding materials for different strain rate and temperature values, phenomenological models of Johnson-Cook, Rule-Jones, Tuazon, Couque are used. In order to observe the influence of yield criteria, the analyses are performed with Von-Mises, Hill48 and Yld2003 yield criteria. To predict the effect of punch velocity and temperature on formability, forming limit diagrams are also obtained for both materials at different conditions. The maximum value of second derivative of strain with respect to time is used as strain localization criterion to predict the necking.

Keywords: Deep drawing, constitutive equations, strain rate, temperature, formability

ÖZ

DERİN ÇEKMEDE DEĞİŞİK BÜNYE DENKLEMLERİ İÇİN GERİNİM HIZI VE SICAKLIĞIN ETKİSİ

Gökşen, Seçkin
Yüksek Lisans, Makina Mühendisliği
Tez Danışmanı: Prof. Dr. Haluk Darendeliler

Ağustos 2019, 105 sayfa

Bu çalışmada, gerinim hızı ve sıcaklığın derin çekme işlemi üzerindeki etkisi farklı akma kriterleri ve pekleşme kuralları kullanılarak incelenmiştir. Bu amaçla farklı gerinim hızı ve sıcaklık değerleri 1 mm kalınlığındaki DKP6112 ve AZ31 sac malzemeler için göz önüne alınmıştır. Sonuçlar, ticari bir sonlu elemanlar programı yardımıyla kalınlık gerinimi dağılımı ve zımba kuvveti değerleri elde edilerek karşılaştırılmıştır. Bahsedilen malzemelerin farklı gerinim hızı ve sıcaklık değerlerindeki bünye denklemleri, Johnson-Cook, Rule-Jones, Tuazon, Couque modelleri ile elde edilmiştir. Akma kriterlerinin etkisi, von Mises, Hill48 ve Yld2003 akma kriterleri kullanılarak belirlenmiştir. Gerinim hızı ve sıcaklığın sac metal şekillendirilebilirliği üzerine etkilerini değerlendirebilmek amacıyla, her iki malzeme için farklı durumlardaki şekillendirilebilirlik şemaları oluşturulmuştur. Boyun verme gerinimin zamana göre ikinci türevinin en yüksek olması kriteri ile tahmin edilmiştir.

Anahtar Kelimeler: Derin çekme, bünye denklemleri, gerinim hızı, sıcaklık, şekillendirilebilirlik

To my loved ones

ACKNOWLEDGEMENTS

I would like to thank my supervisor Prof. Dr. Haluk Darendeliler for his supervision, help and guidance from the beginning to end of this dissertation.

I want to thank Duygu Erdem for her endless support and encouragement throughout this study.

I want to thank my family; Nurten Gökşen, Orhan Gökşen, Seçil Gökşen Uğurer, Selçuk Alp Uğurer and my niece Yasemin Hilal Uğurer for their endless support and encouragement throughout this study.

TABLE OF CONTENTS

LIST OF TABLES

TABLES

LIST OF FIGURES

FIGURES

LIST OF SYMBOLS

SYMBOLS

f	yield function
J_2'	second invariant of deviatoric stress tensor
m	constant according to crystallographic structure for Yld2003-8p
r_0	anisotropy coefficient in rolling direction
r_{45}	anisotropy coefficient in diagonal direction
r_{90}	anisotropy coefficient in transverse direction
T	temperature
T_m	melting temperature
T_r	room temperature
Y_{ref}	reference stress for Yld2003-8p yield criterion
ε_{ij}	strain tensor
ε_{ij}'	deviatoric strain tensor
ε_p	plastic strain
$\dot{\varepsilon}$	strain rate
σ_{ij}	stress tensor
σ_{ij}'	deviatoric stress tensor
σ_0	yield stress in rolling direction
σ_{45}	yield stress in diagonal direction

σ_{90}	yield stress in transverse direction
σ_b	equbiaxial stress
σ_Y	yield stress
θ	angle with respect to rolling direction
σ_θ	stress at angle θ according to rolling direction
λ	plastic multiplier
μ	shear modulus
Δt	step time

CHAPTER 1

INTRODUCTION

1.1. Background and Motivation

Punch velocity that determines the strain rate at each point of deforming sheet is an important process parameter in deep drawing. When the punch velocity is increased, generally limiting drawing ratio and drawability of sheet metal increases. However, thinning in critical regions also increases which makes the sheet being more prone to fail at those regions. For conventional deep drawing operations, punch velocities are in the range between 1 mm/s and 5000 mm/s.

Strain rate is a parameter that affects the stress-strain behavior of the corresponding material. Generally, for quasi-static cases, simple tension tests are conducted with strain rate values ranging between 10^{-4} and 10^{-2} 1/s. For dynamic cases which are performed at higher strain rate values, yield strength of the material increases and stress-strain curve for that material shifts upwards. This means that, for the same strain value, required stresses are higher.

The mechanism and effect of strain rate phenomenon on change of stress-strain behavior is not a fully-understood concept. To take into account the stress-strain behavior with strain rate, there are several constitutive models that updates the stress and strain values according to strain rate value. Using the appropriate constitutive model is crucial for estimating the deformation characteristics of corresponding material. The oldest and the most widely used model among all the others is Johnson-Cook model [1]. To explain strain rate effect in atomic state, Zerilli-Armstrong model

was introduced in 1988 [2]. Later, different models were introduced with modifications of Johnson-Cook and Zerilli-Armstrong models. These models include a number of constants for stress-strain relationship and these constants must be determined experimentally by conducting tension and impact tests with the corresponding strain rate values. For each material used, the experiments must be performed and constants for required model must be determined. It is an important issue to determine the constitutive model and yield criteria that is appropriate for different strain rates and temperatures.

1.2. Objective and Scope of the Thesis

The main aim of the study is to investigate the effect of strain rate and temperature for deep drawing in all aspects. Thickness strain, punch force values are compared for different strain rate and temperature conditions by explicit finite element analyses of different punch configurations. The effects of strain rate and temperature on die geometry are shown. In order to test the effectiveness of different phenomenological constitutive models, thickness strain values are compared for different strain rate and temperature conditions by using corresponding models. To explain the effect of strain rate and temperature on formability characteristics, numerical forming limit diagrams for different conditions are formed.

In this thesis, the effect of strain rate-included constitutive models on deep drawing for hemispherical, cylindrical flat and square punch configurations are investigated at different punch travel values. Two different sheet metals; namely DKP6112 and AZ31 are used with 1 mm thickness for the analyses. These two materials are selected due to experimental material stress-strain data for different strain rate and temperature conditions are available. Analyses are performed by an explicit finite element software [3]. The models are either a built-in or implemented to the finite element software via user material subroutines.

Formability analyses are also performed by the finite element software and forming limit diagrams are built for DKP6112 and AZ31 materials with different strain rate and temperature values by using the criterion of maximum strain acceleration to determine necking time.

1.3. Outline of the Thesis

In the first chapter, a brief introduction, background information and scope of the thesis are given. Chapter 2 gives the literature survey about strain rate and temperature effect on deep drawing. In Chapter 3, theoretical information for plasticity, strain rate-dependent phenomenological models, yield criteria and forming limit diagram are given. In Chapter 4, properties of finite element model used are given. In Chapter 5, the material properties are given for DKP6112 and AZ31 materials. In Chapter 6, the results for different strain rate and temperature-dependent models, different yield criteria are given. Forming limit diagram results are also given for different strain rate and temperature cases. In the last chapter, conclusion of the study and future work are given.

CHAPTER 2

LITERATURE SURVEY

This part of the thesis work is dedicated to conducted research works related to implementation of strain-rate-dependent and temperature-dependent constitutive models for different deep drawing configurations on finite element analysis and comparison with experimental results in the literature. Although there is a vast amount of research work about strain-rate-dependent and temperature-dependent constitutive modelling, there are limited number of works about implementation of these constitutive models for deep drawing process.

Johnson and Cook [1] introduced one of the mostly used phenomenological strain rate and temperature dependent constitutive model. It is valid for strain rates between 0.001 and 1000 s^{-1}. For this range the model gives consistent results with experimental data, however greater values cannot be expressed sufficiently well with this model. Various kinds of materials were studied and material constants were identified for Johnson-Cook model. To identify the material constants, simple tension test data with different strain rate and temperature data is used. The model gives uncoupled effect of strain rate and temperature. The model is the most popular phenomenological model because it gives consistent results for a satisfactory range and it requires relatively low number of constants to be determined.

Zerilli and Armstrong [2] introduced a physically-based strain-rate-dependent constitutive model which explains twinning behavior and strengthening of material through effective grain size refinement. The model was based on thermally-activated dislocation motion. For different crystallographic structure of materials, there are

different models. For face-centered cubic materials, effect of strain, strain rate and temperature are coupled.

Cogun et al. [4] performed analyses of deep drawing process with hemispherical, cylindrical flat and square punch with different hardening models and yield criteria by using ABAQUS Explicit tool. Isotropic, kinematic, combined hardening with von Mises yield criteria were used as hardening models. For yield criterion, Hill48 [5] and updated models such as BBC2008-8p [6] and Yld2003-8p [7] were used. User material subroutine codes were used to implement these updated models to ABAQUS Explicit. To determine model parameters, simple tension tests for rolling and transverse direction and equibiaxial tests were performed for materials SS304 and DKP6112. Thickness strain distribution of cups was compared with all hardening models and yield criterion and it is observed that updated models give better results than the others.

Dizaji et al. [8] developed a new ductile fracture criterion for sheet metal forming processes. Deep drawing for cylindrical flat and square punch was studied with materials SS304, DKP6112 and AA5054 by using ABAQUS/Explicit tool. Proposed fracture criteria was compared with another fracture criterion by using Yld2003-8p [7], BBC2008-8p [6] and Hill48 [5] models on forming limit curves. User material subroutine codes were used to implement these models and fracture criterion to ABAQUS/Explicit. New ductile fracture criteria gave better results than the other fracture criterion.

Ucan [9] used isotropic, kinematic, combined hardening models and Hill48, 3-parameter Barlat model [9] for analyzing cylindrical, square cup drawing and V-bending processes. Analyses were performed with Ls-Dyna tool for the materials St12, SS409 and Al5182. Thickness strain distribution and effective stresses were

compared for different models. Also, earing profiles were compared for different models with different blank holding forces.

Baspinar [10] studied several friction models to identify different contact surface parameter and operating characteristics for deep drawing process. Wilson and Khansori friction models were used. It was observed that Khansori model gives better results for film thickness ratio values below 0.035 and Wilson model gives better results for film thickness ratio values above 0.035. A new combined friction model was built in this study to eliminate the weaknesses of corresponding friction models and combined friction model was developed in MATLAB. Finite element simulations were performed by LS-DYNA.

Panov [11] studied materials stress-strain behavior for several materials with different strain rates and temperatures. A new constitutive model that includes an orthotropic yield criterion, damage growth and failure mechanism was introduced. For strain rate and temperature-dependence, Johnson-Cook [1], Zerilli-Armstrong [2] and Mechanical Threshold Stress [11] model were used. Hill48 model was used for anisotropy characteristics. Material failure modelling was performed by a model compatible with Mechanical Threshold Stress model. AA7010 and OFHC Copper materials were used for this study.

Smerd [12] studied the behavior of aluminum alloys AA5754, AA5182 and AA6111 for strain rates between 600 and 1500 s^{-1} at temperatures between ambient temperature and 300°C. Split Hopkinson pressure bar setup was used. Johnson-Cook [1] and Zerilli-Armstrong [2] models were used for this study. It was observed that Zerilli-Armstrong model gave more accurate results for predicting flow stress. Finite element simulations were performed with LS-DYNA with user subroutine codes. These data

were used in vehicle crash events. It was observed that strain rate increase provided a significant ductility increase.

Yoshida et al. [13] proposed a sixth-order polynomial type 3D yield function. It was the extension of Cazacu-Barlat model. The model was studied for the materials IF Steel, 590 HSS, 780 R HSS and 980 Y HSS. Results from corresponding model were compared with the results from Yld2000-2d [14] and Hill48 [5] models.

Aretz and Barlat [15] proposed two convex yield functions that are called Yld2011-18p (18 parameter) and Yld2011-27p (27 parameter) for planar and three-dimensional stress states. In this study, Yld2011 yield criterion was applied to the sheet materials AA2090-T3, AA3104-H19 and AISI409L. User material subroutine codes were used for implementing these models in ABAQUS/Explicit and ABAQUS/Standart.

Yoon et al. [16] used Yld2000-2d [14] and CPB06ex2 [17] yield functions for earing prediction of cylindrical cup drawing. Tensile tests along 7 directions and cup drawing tests were conducted. Models were studied with AA6111-T4 and AA5042-H2 materials and finite element analyses were also done. CPB06ex2 model predicted 8 ears which was the case of experimental findings.

Comsa and Banabic [6] proposed BBC2008 plane-stress yield function with 8 and 16-parameters to describe the behavior of highly orthotropic materials. They were proposed in order to enhance flexibility of BBC2005 yield criterion. AA2090-T3 material was used for this study. The model predicted more than 4 ears for cylindrical cup drawing.

Yoon et al. [18] implemented Yld2004-18p [18] yield criteria in a finite element analysis for circular blank sheet. For this analysis, AA2090-T3 material was used. In this analysis, 6 ears were predicted with Yld2004-18p which was the case observed in experimental findings. Experimental results and results from Yld2004-18p had a good fit for AA2090-T3 material.

Banabic et al. [19] proposed a new yield function which was the extension BBC2002 [19] yield function. This model was studied for AA2090-T3 and AA6181 material. For determining material constants, simple tension tests and equibiaxial tests were performed.

Aretz [7] proposed Yld2003-8p plane stress with 8 parameters for anisotropic material. In this study, AA2090-T3, AA6111-T4 and low-carbon steel materials were used. Simple tension tests and equibiaxial tests are performed for yield stresses and anisotropy parameters. The model has a similar formulation with Yld2000-2D [14] model. It was observed that the model has the same flexibility of Yld2000-2D and it has a simpler mathematical form and lower computational effort comparing with Yld2000-2D.

Rule and Jones [20] proposed a strain-rate-dependent phenomenological stress-strain relation which is valid for many ductile materials in strain rate values greater than 10^4 s^{-1}. Simple tension tests and high-speed Taylor impact tests are performed for determining material constants. The model is an extension of Johnson-Cook constitutive model. It was studied for the materials Al7075-T6, OFHC copper and wrought iron. It gives better yield and flow stress predictions compared to Johnson-Cook model for high strain rate cases.

Couque [21] proposed a strain rate and temperature dependent phenomenological stress-strain relation for wide range of materials. It included an additional term to Johnson-Cook model. Direct impact Hopkinson pressure bar test setup was used for material parameters. It gave good results for viscous regime which include strain rate values above 10^3.

Tuazon [22] proposed a strain rate and temperature dependent phenomenological stress-strain relation for high strength steels. The model gives good results for strain rate values above 10^4 s^{-1}. It was a variation of Johnson-Cook model. Split Hopkinson pressure bar test setup was used for determining material constants. AISI 4340, Hi-Mn and HSA800 materials were studied.

Salahi and Othman [23] compared six strain-rate-dependent constitutive models which are Huh-Kang [22], Cowper-Symmonds [23], Tuazon [22], Couque [21] and Modified-Eyring models [23]. Three copper and one steel material were used for comparing yield stress values.

Khan and Baig [24] introduced anisotropic constitutive modelling and effects of strain rate and temperature on the formability of aluminum alloys. Khan-Huang-Liang [25] constitutive model was used for strain rate and temperature dependent part. For anisotropy, Barlat's yield function Yld96 was used. AA5182-0 was used for this study.

Varleysen et al. [26] investigated the effect of strain rate on the forming properties for commercial steels CmnAl TRIP, S235JR and drawing steel DC04. Johnson-Cook models were used as constitutive models and Marciniak-Kuczynski method was used for forming limit diagrams. The effect of ductility of the material on forming limit diagram was also studied.

Khan et al. [27] studied quasi-static and dynamic responses of some advanced high strength steels for strain rate values between 10^{-4} and 10^{3} s^{-1}. Split Hopkinson pressure bar setup was used for dynamic tensile testing. TRIP800, DP800 and DQ steel materials were used for this study.

Naka et al. [28] investigated the effects of strain rate, temperature and sheet thickness on the yield locus of AZ31 magnesium-aluminum alloy sheet. Biaxial tests were performed for identifying material parameters. It was observed that the size of yield locus decreases with increasing temperature and decreases with decreasing strain rate. In addition, it was observed that the yield locus of AZ31 sheet for any temperature and strain rate is well described by Barlat-type and Logan-Hosford type models.

Huh et al. [29] introduced the effect of strain rate on plastic anisotropy of advanced high strength steels for strain rate values between 0.001 and 100 s^{-1}. Plastic anisotropy was modelled with Hill48, Yld89 [29] and Yld2000-2d [14]. TRIP and DP-type steel specimens were used for this study. Yield stresses, r-values at various loading angles and yield loci for these materials were given graphically.

Roth and Mohr [30] performed high strain rate tensile experiments for advanced high strength steel materials and the effect of strain rate on ductile fracture initiation was explained. For high strain rate experimentation, split Hopkinson pressure bar setup with high speed photography was used. Johnson-Cook and Swift-Voce model are used with non-associated anisotropic flow. The model was an extension of non-associated quadratic plasticity model of Mohr. The model include 22 material constants.

Han [31] investigated tensile testing with all its aspects. Mechanical behavior in tensile test was explained in detail. In addition, test piece geometry and the necessary tensile test specification ASTM E8 were mentioned. Bauschinger effect on the stress-strain data was explained. In addition, the effects of strain rate and temperature on tensile test data were introduced.

Mamalis et al. [32] performed finite element analyses of cylindrical cup drawing process for different punch velocities, sheet materials density and Coulomb friction coefficients. Different punch velocities and sheet densities were compared according to the impact of computational time. In addition, the working principles of implicit and explicit solving methods were identified in this study.

Shim and Yang [33] performed finite element analysis of deep drawing process in the aspects of membrane and shell elements. It was proposed that shell analysis is more preferable than membrane analysis since membrane theory cannot predict the bending effect. Especially for square cup drawing, shell elements are more preferable.

Jung et al. [34] studied dynamic finite element analysis for sheet metal forming processes for explicit and implicit solving methods and computational time decreasing solutions for these analyses. It was observed that implicit method is more efficient for 2-D analyses. In explicit analysis, the computational time is linearly-independent with problem size. As a result, it is more efficient for large-size problems.

Naka and Yoshida [35] studied the effect of strain rate and temperature for forming behavior of 5083 type aluminum alloy for punch velocities between 0.2 and 500 mm/s. Uniaxial tension and deep drawing test were performed.

Colgan and Monaghan [36] investigated the most important parameters of deep drawing process that are punch and die radii, punch velocity, friction and draw depth. Percent contributions of each factor were calculated by the help of ANOVA software. Punch velocity was the fourth most important parameter for wall thickness deviation.

Seth et al. [37] investigated formability of steel sheet in high velocity impact by electromagnetically launched punch at velocities of 50 and 220 m/s. Experiments were done for 5 different steel specimens with different thicknesses. Failure strains were observed as between 30% and 50%. It was also observed that high forming velocity provides high formability.

Lee et al. [38] investigated the effect of strain rate and temperature on formability of AZ31 alloy sheet for square cup drawing process. It was observed that failures are increased with increasing punch velocity. It was also observed that strain rate effects are more pronounced for higher temperatures.

Ayari et al. [39] performed finite element analysis of a square box to predict the final geometry of drawn cup. Stress, thickness distribution and earing profiles were investigated. It was observed that for this analysis, the results are compliant for experimental findings.

Khan et al. [40] measured AZ31 sheets under uniaxial and multiaxial loadings with different directions in order to explain material behavior of AZ31 alloy for various strain rate and temperature values,. Stress-strain and anisotropy behavior are identified

for 25°C, 65°C, 150°C and 10^{-4}, 10^{-2}, 10^{0} s^{-1} strain rate values in rolling, transverse and diagonal direction.

Khan and Liu [41] investigated the material behavior of Al2024-T351 under uniaxial compression loading. The strain rates include 10^{-4} to 10^{3} s^{-1} and the temperatures of 233 K, 296 K, 358, 422 K and 505 K. To predict the material behavior for different strain rate and temperature values, Khan-Liu phenomenological constitutive model is proposed.

Ma et al. [42] investigated the effect of friction coefficient on deep drawing of aluminum alloy AA6111 at elevated temperatures for three different conditions. Results are compared with the experimental results according to minimum thickness of sheet, thickness distribution and failure mode of formed parts. The optimum value of friction coefficient is determined as 0.15.

Tari et al. [43] analyzed the blank formability of AZ31B magnesium alloy for different strain punch velocity and temperature values. Effect of strain rate and temperature on punch force, thickness distribution and failure are given.

Huang et.al [44] investigated the effect on forming limit of blank thickness and fracture thickness. Fracture strain resulted from uniaxial tension test is used for fracture criterion. Blank is assumed to be fractured when blank thickness is reached fracture thickness in any section. Square cup drawing and elliptical hole flanging are analyzed.

Ozturk and Lee [45] performed prediction of forming limit diagram with different ductile fracture criteria by finite element simulation of out-of-plane formability test. It is observed that fracture predictions for the right side is successful; however for the left side they are not successful according to experimental results. It is also concluded that for fracture prediction ductile fracture criteria could not be used directly.

Karajibani et al. [46] performed Nakazima test simulation with ABAQUS/Explicit for two-layer metallic sheets. Necking time is assumed to be the time at strain acceleration reaches its maximum.

Chalal et al. [47] determined forming limit diagrams with different localization criteria such as criterion of maximum second time derivative of thickness strain, criterion based on the ratio of equivalent plastic strain increment, maximum punch force criterion, loss of ellipticity by using ABAQUS/Explicit tool.

Lumelskyj et al. [48] compared strain localization predictions for numerical and experimental cases. Experimental tests and finite element simulations are performed for DC04 steel material. Maximum strain acceleration method is used as the strain localization criterion. Necking time predictions using maximum strain acceleration method give closer results with experimental case.

CHAPTER 3

THEORETICAL BACKGROUND

3.1. Plasticity

According to Levy-Mises theory of classical plasticity, the relationship between incremental strain and incremental stress can be expressed as [49]:

$$d\varepsilon_{ij} = d\lambda\sigma_{ij}' \tag{3.1}$$

where $d\boldsymbol{\varepsilon}$ is the incremental strain, $\boldsymbol{\sigma}'$ is deviatoric stress and λ is plastic multiplier. Later, a similar equation is given by Prandtl and Reuss:

$$\mathrm{d}\varepsilon_{ij}^{p} = d\lambda\sigma_{ij}' \tag{3.2}$$

where $\mathrm{d}\varepsilon_{ij}^{p}$ is plastic strain increment. Incremental plastic multiplier is determined according to corresponding hardening rule. Mises applied the same idea of complementary strain energy in elasticity theory to plasticity theory that was called plastic potential [49]. Based on plastic potential concept:

$$\mathrm{d}\varepsilon_{ij}^{p} = d\lambda\frac{\partial Q(\sigma_{ij})}{\partial\sigma_{ij}} \tag{3.3}$$

where Q is the scalar function that gives the plastic strains when it is differentiated with respect to stresses. Yield function can be used as the potential function for ductile materials and flow rule can be determined according to this potential function. If potential function is chosen as the yield function, the flow rule is called as associated flow rule. Otherwise, the flow rule is unassociated flow rule. For associated flow rule, incremental stress and strain relation can be expressed as:

$$\mathrm{d}\varepsilon_{ij}^{p} = d\lambda \frac{\partial f}{\partial \sigma_{ij}} \tag{3.4}$$

where f is the yield function. Corresponding yield function represents a surface and incremental plastic strain tensor is perpendicular to this surface. This is called as normality rule. Normality rule has been experimentally confirmed for metals by various experiments [49]. In classical plasticity theory, it is assumed that the volume of the material is constant during deformation. As a result, it is also assumed that the sum of the strain values in three coordinate directions must be zero.

$$\varepsilon_{xx} + \varepsilon_{yy} + \varepsilon_{zz} = 0 \tag{3.5}$$

As the material undergoes plastic deformation, the strain space must remain on the subsequent yield surface. Hence according to the consistency condition:

$$F(\boldsymbol{\sigma} + d\boldsymbol{\sigma}, \boldsymbol{\alpha} + d\boldsymbol{\alpha}) = 0 \tag{3.6}$$

3.2. Phenomenological Stress-strain Relations

3.2.1. Johnson-Cook Model

One of the mostly used model that explains strain rate and temperature effect on stress values is Johnson-Cook model. It is a phenomenological constitutive model. The model is applicable for the range of strain rate values 10^{-3} and 10^{3} [1]. There are different parts that takes strain hardening, strain rate and temperature effects into account as given below:

$$\sigma = (A + B\varepsilon^{n})\left[1 + Cln\left(\frac{\dot{\varepsilon}}{\dot{\varepsilon}_0}\right)\right]\left[1 - \left(\frac{T - T_r}{T_m - T_r}\right)^{m}\right] \tag{3.7}$$

where *A*, *B* and *n* are the strain hardening constants, *C* is the material constant that describes the strain rate characteristic, $\dot{\varepsilon}_0$ is the reference strain rate value which is generally used as 1 in typical application of Johnson-Cook model, *T* is the operating temperature, T_m is the melting temperature of the material. T_r represents the room temperature and *m* is a material constant for temperature-dependent part.

Effects of strain rate and temperature are explained with dimensionless parameters. For strain rate effect, natural logarithm of dimensionless strain rate ratio is used and for temperature effect, dimensionless homologous temperature is used. The constants in the model are determined from stress-strain data for dynamic cases. From the data for different strain rates, a curve fitted to the experimental data by least square regression method. Johnson-Cook model is a powerful method since there is limited amount of constants that must be determined. As a result, it can be considered as a simple-to-implement model and less number of experiments are required to determine these constants. There are huge number of studies that Johnson-Cook constitutive

model has been used to explain strain rate behavior of the materials for different analyses. The model is also implemented on commercial finite element softwares as a built-in function for high strain rate deformation analyses [3].

3.2.2. Zerilli-Armstrong Model

Zerilli and Armstrong [2] reported a model developed for the plastic deformation of body-centered-cubic alpha-iron and face-centered-cubic copper. It is a physically-based model. It is based on thermally activated dislocation motion. The model for materials that have body-centered cubic crystal structure is given as:

$$\sigma = \sigma_G + B_0 e^{\{[-\beta_0+\beta_1 \ln(\dot{\varepsilon})]T\}} + K_0 \varepsilon^n + k_\varepsilon d^{-\frac{1}{2}} \tag{3.8}$$

and that have face-centered cubic crystal structure is given as:

$$\sigma = \sigma_G + B_1 \varepsilon^{1/2} e^{\{[-\beta_0+\beta_1 \ln(\dot{\varepsilon})]T\}} + k_\varepsilon d^{-\frac{1}{2}} \tag{3.9}$$

where σ_G, B_0, β_0, β_1, K_0 and k_ε are the experimental constants based on dislocation mechanics analyses [2]. $\dot{\varepsilon}$ represents operational strain rate and *T* is the temperature. *d* represents the polycrystal grain diameter. For face-centered-cubic materials, $K_0\varepsilon^n$ term is eliminated and the relation between strain and strain rate is coupled. Compared to the other phenomenological models, Zerilli-Armstrong constitutive model explains the deformation twinning phenomenon and this produces strengthening of the material through effective grain size refinement [2]. When the effective grain size decreases, stress values are increasing by the factor of square root of effective grain size.

3.2.3. Rule-Jones Model

Rule and Jones [20] proposed another phenomenological model which takes into account the strain rate and temperature effects. The model gives good results for many ductile materials for strain rates 10^4 or greater. The model which is the modified version of Johnson-Cook model is given in below [20].

$$\sigma = (A + B\varepsilon^n)\left[\left(\frac{\dot{\varepsilon}}{\dot{\varepsilon}_0}\right)^{\alpha}\right]\left[1 - \left(\frac{T - T_r}{T_m - T_r}\right)^m\right] \tag{3.10}$$

where *A*, *B* and *n* are the strain hardening constants. α is the material constant for strain rate. Reference strain rate is generally taken as 1. Temperature-dependent part is the same with Johnson-Cook model. However, it is observed that this model is not widely used. According to that, a revised form of Rule-Jones model is also proposed [20].

$$\sigma = (A + B\varepsilon^n)\left\{1 + C_1 ln\left(\frac{\dot{\varepsilon}}{\dot{\varepsilon}_0}\right) + C_2\left[\frac{1}{C_3 - \ln\left(\frac{\dot{\varepsilon}}{\dot{\varepsilon}_0}\right)} - \frac{1}{C_3}\right]\right\} \left[1 - \left(\frac{T - T_r}{T_m - T_r}\right)^m\right] \tag{3.11}$$

The strain rate sensitivity is expressed better by adding term $1/[C_3\text{-}\ln(\dot{\varepsilon}/\dot{\varepsilon}_0)]$. For low strain rates, strain rate sensitivity term approaches towards zero and Rule-Jones model is reduced to Johnson-Cook model in that region. Results of Rule-Jones model show that they fit well with the experimental findings [20]. It is also observed that for high

strain rates, yield stresses calculated with Rule-Jones constitutive model are greater than the ones estimated from Johnson-Cook model [20].

3.2.4. Huh-Kang Model

Another modification of Johnson-Cook model is proposed by Huh and Kang [22]. A term is added as natural logarithm of square of strain rate ratio value. The equation is given below as:

$$\sigma = (A + B\varepsilon^n)\left[1 + C_1 ln\left(\frac{\dot{\varepsilon}}{\dot{\varepsilon}_0}\right) + C_2 ln\left(\frac{\dot{\varepsilon}}{\dot{\varepsilon}_0}\right)^2\right]\left[1 - \left(\frac{T - T_r}{T_m - T_r}\right)^m\right] \qquad (3.12)$$

where A, B, n, m, C_1 and C_2 are the material constants. Reference strain rate can be considered as 1. Whereas Johnson-Cook model has a linear behavior in logarithmicwise by considering strain rate effect on stress-strain behavior, by the added term, characteristics of strain rate and stress relation becomes quadratic. With this contribution, the effect of strain rate is better explained and for higher strain rates, closer results to the experimental findings are achieved [22].

3.2.5. Modified Johnson-Cook Model

Lin et al. [50] proposed a modified constitutive model which is the combination of Johnson-Cook and Zerilli-Armstrong models:

$$\sigma = (A + B\varepsilon^n)\left[e^{-C_3 T + C_4 T ln\left(\frac{\dot{\varepsilon}}{\dot{\varepsilon}_0}\right)}\right]\left[1 - \left(\frac{T - T_r}{T_m - T_r}\right)^m\right] \qquad (3.13)$$

Where *A*, *B*, *n*, *m*, C_3 and C_4 are the material constants. Reference strain rate is taken as 1 [50]. The material constants are determined from curve fitting technique for the data taken from hot compression test [50]. Proposed constitutive model combines strain hardening portion of Johnson-Cook model and strain rate portion of Zerilli-Armstrong model. The model includes the coupled effects of temperature and strain rate. Model is suitable for high strain rate hot forming processes. The model is studied in hot compression test between 850-1150°C and strain rate values between 1-50 s^{-1} [50]. For this region, the model works very well for these temperature values whereas Johnson-Cook and Zerilli-Armstrong models have significant deviations.

3.2.6. Couque Model

Couque [21] proposed a strain rate and temperature-dependent model. In this study, strain rate values between 10^{-3} and 10^5 are investigated. It is observed that Johnson-Cook model fits well with experimental data for thermally activated regime (strain rates values 10^{-3} and 10^3) [1]. However, it is also observed that for viscous regime (strain rate values 10^3 and 10^5) deviation of Johnson-Cook model from experimental results is significantly greater. To reflect the behavior of material in viscous regime better, an additional power of strain rate term is added to Johnson-Cook constitutive model [21], as shown below:

$$\sigma = (A + B\varepsilon^n)\left[1 + C_1 ln\left(\frac{\dot{\varepsilon}}{\dot{\varepsilon}_0}\right) + D ln\left(\frac{\dot{\varepsilon}}{\dot{\varepsilon}_1}\right)^k\right]\left[1 - \left(\frac{T - T_r}{T_m - T_r}\right)^m\right] \qquad (3.14)$$

where *A*, *B*, *n*, *m*, *C*, *D* and *k* are the material constants. Reference strain rates $\dot{\varepsilon}_0$ and $\dot{\varepsilon}_1$ can be considered as 1 and 10^3 1/s respectively. For thermally activated regime, the last term in the group of strain rate terms has negligible effect. It can be stated that for

this region, the model gives similar results to Johnson-Cook model. For viscous regime, the last term dominates the strain-rate behavior of the material [21]. As a result, the model gives good results for relatively higher speed deformation processes.

For determining the constants stated in the model, high speed tensile testing must be performed. For this, Direct Hopkinson Pressure Bar method is used for high strain rate tensile testing.

3.2.7. Tuazon Model

Tuazon et al. [22] proposed another constitutive model which is also a variation of Johnson-Cook model. The model works well by the range of the strain rates 10^{-3} and 10^{4}. The model is given as:

$$\sigma = (A + B\varepsilon^{n})\left[1 + Cln\left(\frac{\dot{\varepsilon}}{\dot{\varepsilon_0}}\right)^{p}\right]\left[1 - \left(\frac{T - T_r}{T_m - T_r}\right)^{m}\right] \tag{3.15}$$

where *A*, *B*, *n*, *C* and *p* are the material constants. Reference strain rate is considered as 1. With modification of strain-rate-dependent term into its power, the linear behavior yield stress estimation Johnson-Cook model is eliminated. For higher strain rate values, this behavior deviates significantly from experimental findings. For new modified model, yield stresses in high strain rate deformations are closely estimated [22]. For determining the constants stated in the model, high speed tensile testing procedures must be followed.

3.3. Yield Criteria

A yield criterion is one of the essential part for expressing a constitutive model. In this study, Von-Mises, Hill48 and Yld2003-8p are used for the analyses with different punch configurations.

3.3.1. Von Mises Yield Criterion

Von-Mises yield criterion [49] is one of the oldest and mostly used yield criterion in plasticity applications. The criterion assumes that plastic yielding will occur only when the second invariant $J_2^{'}$ of the deviatoric stress tensor reaches a critical value κ^2 as given below:

$$J_2' - \kappa^2 = 0 \tag{3.16}$$

In terms stress components, the criterion can be written as:

$$\left[\left(\sigma_{xx} - \sigma_{yy}\right)^2 + \left(\sigma_{yy} - \sigma_{zz}\right)^2 + (\sigma_{zz} - \sigma_{xx})^2 + {\sigma_{xy}}^2 + {\sigma_{yz}}^2 + {\sigma_{xz}}^2\right] = \kappa^2 \tag{3.17}$$

Whereas in terms of principal stresses, it is given as:

$$\frac{1}{6}[(\sigma_1 - \sigma_2)^2 + (\sigma_2 - \sigma_3)^2 + (\sigma_3 - \sigma_1)^2] = \kappa^2 \tag{3.18}$$

Using the simple tension test, constant κ can be determined as $\sigma_Y/\sqrt{3}$ where σ_Y is the yield stress in simple tension. Then,

$$\frac{3}{2}\sigma_{ij}{}'\sigma_{ij}{}' = \sigma_Y{}^2 \tag{3.19}$$

The corresponding equivalent plastic strain is given as:

$$\bar{\varepsilon}_p = \sqrt{\frac{2}{3}\varepsilon_{ij}{}^p\varepsilon_{ij}{}^p} \tag{3.20}$$

For Von-Mises yield criterion, yield surface is a cylinder parallel to the hydrostatic axis and its locus on the π-plane is a circle. ABAQUS uses Von-Mises yield criterion for all plastic analyses unless otherwise specified.

3.3.2. Hill48 Yield Criterion

Hill48 yield criterion [5] is one of the mostly used yield criterion for orthotropic materials. This criterion assumes that hydrostatic stress has no effect on yielding and Bauschinger effect is not considered. The yield function of can be written as:

$$\begin{aligned} 2f(\sigma_{ij}) = F(\sigma_{yy}-\sigma_{zz})^2 + G(\sigma_{zz}-\sigma_{xx})^2 + H(\sigma_{xx}-\sigma_{yy})^2 \\ + 2L\sigma_{yz}{}^2 + 2M\sigma_{xz}{}^2 + 2N\sigma_{xy}{}^2 - 1 = 0 \end{aligned} \tag{3.21}$$

where *F*, *G*, *H*, *L*, *M* and *N* are material constants describing the state of anisotropic behavior. In order to determine the constants *F*, *G* and *H*, the tensile yield strength values for three principal directions of anisotropy must be measured. Then,

$$\frac{1}{X^2} = G + H \tag{3.22}$$

$$\frac{1}{Y^2} = H + F \tag{3.23}$$

$$\frac{1}{Z^2} = F + G \tag{3.24}$$

where *X*, *Y*, *Z* are the tensile yield stresses for corresponding principal directions. Solving for *F*, *G* and *H*:

$$F = \frac{1}{2}\left(\frac{1}{Y^2} + \frac{1}{Z^2} - \frac{1}{X^2}\right) \tag{3.25}$$

$$G = \frac{1}{2}\left(\frac{1}{Z^2} + \frac{1}{X^2} - \frac{1}{Y^2}\right) \tag{3.26}$$

$$H = \frac{1}{2}\left(\frac{1}{Y^2} + \frac{1}{X^2} - \frac{1}{Z^2}\right) \tag{3.27}$$

To determine the constants *L*, *M*, *N*, the yield stresses for pure shear *R*, *S* and *T* on each of the orthogonal planes of anisotropy *yz*, *xz* and *xy* should be determined:

$$L = \frac{1}{2R^2} \qquad M = \frac{1}{2S^2} \qquad N = \frac{1}{2T^2} \tag{3.28}$$

According to Hill48 yield criterion, associated flow rule for principal strain values:

$$d\varepsilon_{xx}{}^{p} = d\lambda[H(\sigma_{xx} - \sigma_{yy}) + G(\sigma_{xx} - \sigma_{zz})] \tag{3.29}$$

$$d\varepsilon_{yy}{}^{p} = d\lambda[H(\sigma_{xx} - \sigma_{yy}) + F(\sigma_{yy} - \sigma_{zz})] \tag{3.30}$$

$$d\varepsilon_{zz}{}^{p} = d\lambda[G(\sigma_{zz} - \sigma_{xx}) + F(\sigma_{zz} - \sigma_{yy})] \tag{3.31}$$

Lankford anisotropy coefficients r_0, r_{90} and r_{45} [8] can be expressed as

$$r_0 = \frac{H}{G} \tag{3.32}$$

$$r_{45} = \frac{N}{F+G} - \frac{1}{2} \tag{3.33}$$

$$r_{90} = \frac{H}{F} \tag{3.34}$$

Then, using these coefficients and $X = \sigma_0$, $Y = \sigma_{90}$, $Z = \sigma_{45}$ where σ_0, σ_{90} and σ_{45} is the yield strength values in different directions, the yield criterion for plane stress condition is given as [8]:

$$\begin{aligned} {\sigma_{xx}}^2 - \frac{2r_0}{1+r_0}\sigma_{xx}\sigma_{yy} + \frac{r_0(1+r_{90})}{r_{90}(1+r_0)}{\sigma_{yy}}^2 \\ + \frac{r_0 + r_{90}}{r_{90}(1+r_0)}(2r_{45}+1){\sigma_{xy}}^2 = {\sigma_0}^2 \end{aligned} \tag{3.35}$$

3.3.3. Yld2003-8p Yield Criterion

Yld2003 yield criterion was proposed by Aretz [7]. The yield criterion involves eight anisotropy parameters that can be determined from experimental procedures. According to proposed model by Aretz [7], a_8 is taken as 1 to eliminate the test procedure for determining r_b. The function is generalized from the Hosford's non-quadratic yield function:

$$|\sigma_{11} - \sigma_{22}|^m + |\sigma_{22} - \sigma_{33}|^m + |\sigma_{33} - \sigma_{11}|^m = 2{Y_{ref}}^m \tag{3.36}$$

where *m* is a constant determined according to the crystallographic structure of the material. For plane stress condition (σ_{33}= 0) and in terms of principal stresses Hosford's function can be written as:

$$|\sigma_1 - \sigma_2|^m + |\sigma_2|^m + |\sigma_1|^m = 2{Y_{ref}}^m \tag{3.37}$$

Aretz generalized corresponding yield function and proposed the new yield criterion:

$$|\sigma_1'' - \sigma_2''|^m + |\sigma_2'|^m + |\sigma_1'|^m = 2{Y_{ref}}^m \tag{3.38}$$

where

$$\sigma_{1,2}' = \frac{a_8\sigma_{11} + a_1\sigma_{22}}{2} \pm \sqrt{\left(\frac{a_2\sigma_{11} - a_3\sigma_{22}}{2}\right)^2 + {a_4}^2\sigma_{12}\sigma_{21}} \tag{3.39}$$

$$\sigma_{1,2}'' = \frac{\sigma_{11} + \sigma_{22}}{2} \pm \sqrt{\left(\frac{a_5\sigma_{11} - a_6\sigma_{22}}{2}\right)^2 + {a_7}^2\sigma_{12}\sigma_{21}} \tag{3.40}$$

For Yld2003 the equivalent stress can be calculated as:

$$\bar{\sigma} = \left[\frac{1}{2}(|\sigma_1'' - \sigma_2''|^m + |\sigma_2'|^m + |\sigma_1'|^m)\right]^{\frac{1}{m}} \tag{3.41}$$

Then the yield function can be expressed as:

$$f(a_i, \sigma) = \bar{\sigma}(a_i, \sigma) - Y_{ref} \tag{3.42}$$

The eight anisotropy parameters, σ_0, σ_{45}, σ_{90}, r_0, r_{45}, σ_{90}, σ_b and r_b must be found from related experimental work. For sheet metal forming processes, Y_{ref} is generally considered as being equal with σ_0. From the tensor transformation rules, the stress components can be written in terms of σ_θ using angle θ from the rolling direction:

$$\sigma_{11} = \sigma_\theta \, cos^2\theta \tag{3.43}$$

$$\sigma_{22} = \sigma_\theta \, sin^2\theta \tag{3.44}$$

$$\sigma_{12} = \sigma_\theta \, sin\theta \, cos\theta \tag{3.45}$$

In rolling direction where θ = 0˚, following relations can be determined according to expressions given in Eq. (3.39) and Eq. (3.40):

$$\sigma_{11} = \sigma_0 \qquad \sigma_{22} = 0 \qquad \sigma_{12} = 0 \tag{3.46}$$

$$\sigma_1{}' = \frac{\sigma_0}{2} + \frac{a_2\sigma_0}{2} \tag{3.47}$$

$$\sigma_2{}' = \frac{\sigma_0}{2} - \frac{a_2\sigma_0}{2} \tag{3.48}$$

$$\sigma_1'' = \frac{\sigma_0}{2} + \frac{a_5\sigma_0}{2} \tag{3.49}$$

$$\sigma_2'' = \frac{\sigma_0}{2} - \frac{a_5\sigma_0}{2} \tag{3.50}$$

For transverse direction θ = 90˚is,

$$\sigma_{11} = 0 \qquad \sigma_{22} = \sigma_{90} \qquad \sigma_{12} = 0 \tag{3.51}$$

$$\sigma_1' = \frac{a_1\sigma_{90}}{2} + \frac{a_3\sigma_{90}}{2} \tag{3.52}$$

$$\sigma_2' = \frac{a_1\sigma_{90}}{2} - \frac{a_3\sigma_{90}}{2} \tag{3.53}$$

$$\sigma_1'' = \frac{\sigma_{90}}{2} + \frac{a_6\sigma_{90}}{2} \tag{3.54}$$

$$\sigma_2'' = \frac{\sigma_{90}}{2} - \frac{a_6\sigma_{90}}{2} \tag{3.55}$$

For diagonal direction θ = 45˚is,

$$\sigma_{11} = \frac{1}{2}\sigma_{45} \qquad \sigma_{22} = \frac{1}{2}\sigma_{45} \qquad \sigma_{12} = \frac{1}{2}\sigma_{45} \tag{3.56}$$

$$\sigma_1{}' = \frac{1}{4}\sigma_{45}(1 + a_1) + \left[\left(\frac{1}{4}\sigma_{45}(a_2 - a_3)\right)^2 + \frac{1}{4}{\sigma_{45}}^2{a_4}^2\right]^{\frac{1}{2}} \tag{3.57}$$

$$\sigma_2{}' = \frac{1}{4}\sigma_{45}(1 + a_1) - \left[\left(\frac{1}{4}\sigma_{45}(a_2 - a_3)\right)^2 + \frac{1}{4}{\sigma_{45}}^2{a_4}^2\right]^{\frac{1}{2}} \tag{3.58}$$

$$\sigma_1{}'' = \frac{1}{4}\sigma_{45} + \left[\left(\frac{1}{4}\sigma_{45}(a_5 - a_6)\right)^2 + \frac{1}{4}{a_7}^2\right]^{\frac{1}{2}} \tag{3.59}$$

$$\sigma_2{}'' = \frac{1}{4}\sigma_{45} - \left[\left(\frac{1}{4}\sigma_{45}(a_5 - a_6)\right)^2 + \frac{1}{4}{a_7}^2\right]^{\frac{1}{2}} \tag{3.60}$$

For steel materials *m* is considered as 6. For DKP Steel in rolling direction, yield function becomes as follows according to Eq. (3.41).

$$\left\{\frac{1}{2}\left(\left|\frac{a_0(1 + a_5)}{2}\right|^6 + \left|\frac{\sigma_0}{2} - \frac{a_2\sigma_0}{2}\right|^6 + \left|\frac{\sigma_0}{2} + \frac{a_2\sigma_0}{2}\right|^6\right)\right\}^{\frac{1}{6}} - \sigma_0 = 0 \tag{3.61}$$

Yield function for diagonal direction θ = 90˚is,

$$\left\{\frac{1}{2}\left(\left|\frac{a_{90}(1+a_6)}{2}\right|^6+\left|\frac{a_1\sigma_{90}}{2}-\frac{a_3\sigma_{90}}{2}\right|^6+\left|\frac{a_1\sigma_{90}}{2}+\frac{a_3\sigma_{90}}{2}\right|^6\right)\right\}^{\frac{1}{6}}-\sigma_0=0 \quad (3.62)$$

Yield function for diagonal direction θ = 45˚is,

$$\begin{aligned}\left\{\frac{1}{2}\left(\frac{a_{45}(1+a_1)}{4}+\left[\left(\frac{a_{45}(a_2-a_3)}{4}\right)^2+\frac{a_{45}\,{a_4}^2}{4}\right]^{\frac{1}{2}}\right)^6\right.\\ +\left(\frac{a_{45}(1+a_1)}{4}-\left[\left(\frac{a_{45}(a_2-a_3)}{4}\right)^2+\frac{a_{45}\,{a_4}^2}{4}\right]^{\frac{1}{2}}\right)^6\\ +\left[\frac{a_{45}}{4}+\left[\left(\frac{a_{45}(a_5-a_6)}{4}\right)^2+\frac{a_{45}\,{a_7}^2}{4}\right]^{\frac{1}{2}}-\frac{a_{45}}{4}\right.\\ \left.\left.+\left[\left(\frac{a_{45}(a_5-a_6)}{4}\right)^2+\frac{a_{45}\,{a_7}^2}{4}\right]^{\frac{1}{2}}\right]^6\right\}^{\frac{1}{6}}-\sigma_0=0\end{aligned} \quad (3.63)$$

To obtain the other necessary equations, the expressions for anisotropy coefficients must be investigated [8]:

$$r_0 = -\left(\frac{\frac{\partial f}{\partial \sigma_{22}}}{\frac{\partial f}{\partial \sigma_{11}} + \frac{\partial f}{\partial \sigma_{22}}} \right)_{\sigma_0} \tag{3.64}$$

$$r_{90} = -\left(\frac{\frac{\partial f}{\partial \sigma_{11}}}{\frac{\partial f}{\partial \sigma_{11}} + \frac{\partial f}{\partial \sigma_{22}}} \right)_{\sigma_{90}} \tag{3.65}$$

$$r_{45} = -\left(\frac{\frac{1}{2}\frac{\partial f}{\partial \sigma_{11}} - \frac{\partial f}{\partial \sigma_{12}} + \frac{1}{2}\frac{\partial f}{\partial \sigma_{22}}}{\frac{\partial f}{\partial \sigma_{11}} + \frac{\partial f}{\partial \sigma_{22}}} \right)_{\sigma_{45}} \tag{3.66}$$

$$\bar{\sigma}^{2k} = \hat{\sigma} \qquad f = \frac{\bar{\sigma}^{2k}}{{Y_{ref}}^{2k}} - 1 = 0 \qquad \frac{\partial f}{\partial \hat{\sigma}} = \frac{1}{{Y_{ref}}^{2k}} \tag{3.67}$$

Where $m = 2k$. General form of the derivative can be obtained as in the following [8]:

$$\frac{\partial F}{\partial \sigma_{11}} = \frac{\partial f}{\partial \hat{\sigma}} \left[\frac{\partial \hat{\sigma}}{\partial \sigma_1'} \frac{\partial \sigma_1'}{\partial \sigma_{11}} + \frac{\partial \hat{\sigma}}{\partial \sigma_2'} \frac{\partial \sigma_2'}{\partial \sigma_{11}} + \frac{\partial \hat{\sigma}}{\partial \sigma_1''} \frac{\partial \sigma_1''}{\partial \sigma_{11}} + \frac{\partial \hat{\sigma}}{\partial \sigma_2''} \frac{\partial \sigma_2''}{\partial \sigma_{11}} \right] \tag{3.68}$$

$$\frac{\partial F}{\partial \sigma_{22}} = \frac{\partial f}{\partial \hat{\sigma}} \left[\frac{\partial \hat{\sigma}}{\partial \sigma_1'} \frac{\partial \sigma_1'}{\partial \sigma_{22}} + \frac{\partial \hat{\sigma}}{\partial \sigma_2'} \frac{\partial \sigma_2'}{\partial \sigma_{22}} + \frac{\partial \hat{\sigma}}{\partial \sigma_1''} \frac{\partial \sigma_1''}{\partial \sigma_{22}} + \frac{\partial \hat{\sigma}}{\partial \sigma_2''} \frac{\partial \sigma_2''}{\partial \sigma_{22}} \right] \tag{3.69}$$

$$\frac{\partial F}{\partial \sigma_{12}} = \frac{\partial f}{\partial \hat{\sigma}}\left[\frac{\partial \hat{\sigma}}{\partial \sigma_1'}\frac{\partial \sigma_1'}{\partial \sigma_{12}} + \frac{\partial \hat{\sigma}}{\partial \sigma_2'}\frac{\partial \sigma_2'}{\partial \sigma_{12}} + \frac{\partial \hat{\sigma}}{\partial \sigma_1''}\frac{\partial \sigma_1''}{\partial \sigma_{12}} + \frac{\partial \hat{\sigma}}{\partial \sigma_2''}\frac{\partial \sigma_2''}{\partial \sigma_{12}}\right] \tag{3.70}$$

$$\frac{\partial \bar{\sigma}}{\partial \sigma_1'} = \frac{1}{2}m|\sigma_1'|^{m-1} = 3|\sigma_1'|^5 \qquad \frac{\partial \bar{\sigma}}{\partial \sigma_2'} = 3|\sigma_2'|^5 \tag{3.71}$$

$$\frac{\partial \sigma_1'}{\partial \sigma_{11}} = \frac{1}{2} + \frac{1}{2}\left[\left(\frac{a_2\sigma_{11} - a_3\sigma_{22}}{2}\right)^2 + a_4^2\sigma_{12}^2\right]^{-\frac{1}{2}}\left(\frac{a_2^2\sigma_{11} - a_2a_3\sigma_{22}}{2}\right) \tag{3.72}$$

$$\frac{\partial \sigma_2'}{\partial \sigma_{11}} = \frac{1}{2} - \frac{1}{2}\left[\left(\frac{a_2\sigma_{11} - a_3\sigma_{22}}{2}\right)^2 + a_4^2\sigma_{12}^2\right]^{-\frac{1}{2}}\left(\frac{a_2^2\sigma_{11} - a_2a_3\sigma_{22}}{2}\right) \tag{3.73}$$

$$\frac{\partial \sigma_1'}{\partial \sigma_{22}} = \frac{1}{2}a_1 + \frac{1}{2}\left[\left(\frac{a_2\sigma_{11} - a_3\sigma_{22}}{2}\right)^2 + a_4^2\sigma_{12}^2\right]^{-\frac{1}{2}}\left(\frac{a_3^2\sigma_{22} - a_2a_3\sigma_{11}}{2}\right) \tag{3.74}$$

$$\frac{\partial \sigma_1'}{\partial \sigma_{12}} = \frac{1}{2}\left[\left(\frac{a_2\sigma_{11} - a_3\sigma_{22}}{2}\right)^2 + a_4^2\sigma_{12}^2\right]^{-\frac{1}{2}}2a_4^2\sigma_{12} \tag{3.75}$$

$$\frac{\partial \sigma_2'}{\partial \sigma_{22}} = \frac{1}{2}a_1 - \frac{1}{2}\left[\left(\frac{a_2\sigma_{11} - a_3\sigma_{22}}{2}\right)^2 + a_4^2\sigma_{12}^2\right]^{-\frac{1}{2}}\left(\frac{a_3^2\sigma_{22} - a_2a_3\sigma_{11}}{2}\right) \tag{3.76}$$

$$\frac{\partial \sigma_2'}{\partial \sigma_{12}} = -\frac{1}{2}\left[\left(\frac{a_2\sigma_{11} - a_3\sigma_{22}}{2}\right)^2 + a_4^2\sigma_{12}^2\right]^{-\frac{1}{2}}2a_4^2\sigma_{12} \tag{3.77}$$

$$\frac{\partial \sigma_1''}{\partial \sigma_{11}} = \frac{1}{2} + \frac{1}{2}\left[\left(\frac{a_5\sigma_{11} - a_6\sigma_{22}}{2}\right)^2 + a_7^2\sigma_{12}^2\right]^{-\frac{1}{2}}\left(\frac{a_5^2\sigma_{11} - a_2a_3\sigma_{22}}{2}\right) \quad (3.78)$$

$$\frac{\partial \sigma_1''}{\partial \sigma_{22}} = \frac{1}{2} + \frac{1}{2}\left[\left(\frac{a_5\sigma_{11} - a_6\sigma_{22}}{2}\right)^2 + a_7^2\sigma_{12}^2\right]^{-\frac{1}{2}}\left(\frac{a_6^2\sigma_{22} - a_5a_6\sigma_{11}}{2}\right) \quad (3.79)$$

$$\frac{\partial \sigma_1''}{\partial \sigma_{12}} = \frac{1}{2}\left[\left(\frac{a_5\sigma_{11} - a_6\sigma_{22}}{2}\right)^2 + a_7^2\sigma_{12}^2\right]^{-\frac{1}{2}} 2a_7^2\sigma_{12} \quad (3.80)$$

$$\frac{\partial \sigma_2''}{\partial \sigma_{12}} = -\frac{1}{2}\left[\left(\frac{a_5\sigma_{11} - a_6\sigma_{22}}{2}\right)^2 + a_7^2\sigma_{12}^2\right]^{-\frac{1}{2}} 2a_7^2\sigma_{12} \quad (3.81)$$

$$\frac{\partial \sigma_2''}{\partial \sigma_{11}} = \frac{1}{2} - \frac{1}{2}\left[\left(\frac{a_5\sigma_{11} - a_6\sigma_{22}}{2}\right)^2 + a_7^2\sigma_{12}^2\right]^{-\frac{1}{2}}\left(\frac{a_5^2\sigma_{11} - a_5a_6\sigma_{22}}{2}\right) \quad (3.82)$$

$$\frac{\partial \sigma_2''}{\partial \sigma_{22}} = \frac{1}{2} - \frac{1}{2}\left[\left(\frac{a_5\sigma_{11} - a_6\sigma_{22}}{2}\right)^2 + a_7^2\sigma_{12}^2\right]^{-\frac{1}{2}}\left(\frac{a_6^2\sigma_{22} - a_5a_6\sigma_{11}}{2}\right) \quad (3.83)$$

For $\theta = 0^\circ$:

$$\frac{\partial \sigma_1'}{\partial \sigma_{11}} = \frac{1}{2} + \frac{1}{2} a_2 \tag{3.84}$$

$$\frac{\partial \sigma_2'}{\partial \sigma_{11}} = \frac{1}{2} - \frac{1}{2} a_2 \tag{3.85}$$

$$\frac{\partial \sigma_1'}{\partial \sigma_{22}} = \frac{1}{2} a_1 + \frac{1}{2} a_2 \tag{3.86}$$

$$\frac{\partial \sigma_1'}{\partial \sigma_{12}} = 0 \tag{3.87}$$

$$\frac{\partial \sigma_2'}{\partial \sigma_{22}} = \frac{1}{2} a_1 + \frac{1}{2} a_3 \tag{3.88}$$

$$\frac{\partial \sigma_2'}{\partial \sigma_{12}} = 0 \tag{3.89}$$

$$\frac{\partial \sigma_1''}{\partial \sigma_{11}} = \frac{1}{2} + \frac{1}{2} a_5 \tag{3.90}$$

$$\frac{\partial \sigma_1''}{\partial \sigma_{22}} = \frac{1}{2} - \frac{1}{2} a_6 \tag{3.91}$$

$$\frac{\partial \sigma_1''}{\partial \sigma_{12}} = 0 \tag{3.92}$$

$$\frac{\partial \sigma_2''}{\partial \sigma_{12}} = 0 \tag{3.93}$$

$$\frac{\partial \sigma_2''}{\partial \sigma_{11}} = \frac{1}{2} - \frac{1}{2} a_5 \tag{3.94}$$

$$\frac{\partial \sigma_2''}{\partial \sigma_{22}} = \frac{1}{2} + \frac{1}{2} a_6 \tag{3.95}$$

For θ = 90°:

$$\frac{\partial \sigma_1'}{\partial \sigma_{22}} = \frac{1}{2} a_1 + \frac{1}{2} a_3 \tag{3.96}$$

$$\frac{\partial \sigma_2'}{\partial \sigma_{22}} = \frac{1}{2} a_1 - \frac{1}{2} a_3 \tag{3.97}$$

$$\frac{\partial \sigma_1''}{\partial \sigma_{22}} = \frac{1}{2} + \frac{1}{2} a_6 \tag{3.98}$$

$$\frac{\partial \sigma_2''}{\partial \sigma_{22}} = \frac{1}{2} - \frac{1}{2} a_6 \tag{3.99}$$

$$\frac{\partial \sigma_1'}{\partial \sigma_{11}} = \frac{1}{2} - \frac{1}{2} a_2 \tag{3.100}$$

$$\frac{\partial \sigma_2'}{\partial \sigma_{11}} = \frac{1}{2} + \frac{1}{2} a_2 \tag{3.101}$$

$$\frac{\partial \sigma_1''}{\partial \sigma_{11}} = \frac{1}{2} - \frac{1}{2} a_6 \tag{3.102}$$

$$\frac{\partial \sigma_1''}{\partial \sigma_{11}} = \frac{1}{2} - \frac{1}{2} a_5 \tag{3.103}$$

$$\frac{\partial \sigma_2''}{\partial \sigma_{11}} = \frac{1}{2} + \frac{1}{2} a_5 \tag{3.104}$$

$$\frac{\partial \sigma_1'}{\partial \sigma_{12}} = \frac{\partial \sigma_2'}{\partial \sigma_{12}} = \frac{\partial \sigma_1''}{\partial \sigma_{12}} = \frac{\partial \sigma_2''}{\partial \sigma_{12}} = 0 \tag{3.105}$$

For θ = 45°:

$$\frac{\partial \sigma_1'}{\partial \sigma_{11}} = \frac{1}{2} + \frac{1}{2}\left[\left(\frac{\sigma_{45}a_2 - \sigma_{45}a_3}{4}\right)^2 + \frac{\sigma_{45}}{4}a_4^2\right]^{-\frac{1}{2}}\left(\frac{\sigma_{45}a_2^2 - \sigma_{45}a_2a_3}{4}\right) \quad (3.106)$$

$$\frac{\partial \sigma_2'}{\partial \sigma_{11}} = \frac{1}{2} - \frac{1}{2}\left[\left(\frac{\sigma_{45}a_2 - \sigma_{45}a_3}{4}\right)^2 + \frac{\sigma_{45}}{4}a_4^2\right]^{-\frac{1}{2}}\left(\frac{\sigma_{45}a_2^2 - \sigma_{45}a_2a_3}{4}\right) \quad (3.107)$$

$$\frac{\partial \sigma_1'}{\partial \sigma_{22}} = \frac{1}{2}a_1 + \frac{1}{2}\left[\left(\frac{\sigma_{45}a_2 - \sigma_{45}a_3}{4}\right)^2 + \frac{\sigma_{45}}{4}a_4^2\right]^{-\frac{1}{2}}\left(\frac{\sigma_{45}a_3^2 - \sigma_{45}a_2a_3}{4}\right) \quad (3.108)$$

$$\frac{\partial \sigma_1'}{\partial \sigma_{12}} = -\frac{1}{2}\left[\left(\frac{\sigma_{45}a_2 - \sigma_{45}a_3}{4}\right)^2 + \frac{\sigma_{45}^2}{4}a_4^2\right]^{-\frac{1}{2}}(\sigma_{45}a_4^2) \quad (3.109)$$

$$\frac{\partial \sigma_1''}{\partial \sigma_{11}} = \frac{1}{2} + \frac{1}{2}\left[\left(\frac{\sigma_{45}a_5 - \sigma_{45}a_6}{4}\right)^2 + \frac{\sigma_{45}^2}{4}a_7^2\right]^{-\frac{1}{2}}\left(\frac{\sigma_{45}a_5^2 - \sigma_{45}a_5a_6}{4}\right) \quad (3.110)$$

$$\frac{\partial \sigma_1''}{\partial \sigma_{22}} = \frac{1}{2} + \frac{1}{2}\left[\left(\frac{\sigma_{45}a_5 - \sigma_{45}a_6}{4}\right)^2 + \frac{\sigma_{45}^2}{4}a_7^2\right]^{-\frac{1}{2}}\left(\frac{\sigma_{45}a_6^2 - \sigma_{45}a_5a_6}{4}\right) \quad (3.111)$$

$$\frac{\partial \sigma_1''}{\partial \sigma_{12}} = \frac{1}{2}\left[\left(\frac{\sigma_{45}a_5 - \sigma_{45}a_6}{4}\right)^2 + \frac{\sigma_{45}^2}{4}a_7^2\right]^{-\frac{1}{2}}(\sigma_{45}a_7^2) \quad (3.112)$$

$$\frac{\partial \sigma_2''}{\partial \sigma_{12}} = -\frac{1}{2}\left[\left(\frac{\sigma_{45}a_5 - \sigma_{45}a_6}{4}\right)^2 + \frac{\sigma_{45}^2}{4}a_7^2\right]^{-\frac{1}{2}}(\sigma_{45}a_7^2) \tag{3.113}$$

$$\frac{\partial \sigma_2''}{\partial \sigma_{11}} = \frac{1}{2} - \frac{1}{2}\left[\left(\frac{\sigma_{45}a_5 - \sigma_{45}a_6}{4}\right)^2 + \frac{\sigma_{45}^2}{4}a_7^2\right]^{-\frac{1}{2}}\left(\frac{\sigma_{45}a_5^2 - \sigma_{45}a_5a_6}{4}\right) \tag{3.114}$$

$$\frac{\partial \sigma_2''}{\partial \sigma_{22}} = \frac{1}{2} - \frac{1}{2}\left[\left(\frac{\sigma_{45}a_5 - \sigma_{45}a_6}{4}\right)^2 + \frac{\sigma_{45}^2}{4}a_7^2\right]^{-\frac{1}{2}}\left(\frac{\sigma_{45}a_6^2 - \sigma_{45}a_5a_6}{4}\right) \tag{3.115}$$

For the final equation, equibiaxial condition must be considered:

$$\sigma_{11} = \sigma_{22} = \sigma_b \qquad \sigma_{12} = \sigma_{21} = 0 \tag{3.116}$$

$$\sigma_1' = \frac{\sigma_b}{2}[1 + a_1 + |a_2 - a_3|] \tag{3.117}$$

$$\sigma_2' = \frac{\sigma_b}{2}[1 + a_1 + |a_2 - a_3|^2] \tag{3.118}$$

$$\sigma_1'' = \frac{\sigma_b}{2}[2 + |a_5 - a_6|] \tag{3.119}$$

$$\sigma_2'' = \frac{\sigma_b}{2}[2 - |a_5 - a_6|] \tag{3.120}$$

$$\left\{\frac{1}{2}\left[\frac{\sigma_b}{2}(1 + a_1 + |a_2 - a_3|)\right]^6 + \left[\frac{\sigma_b}{2}(1 + a_1 + |a_2 - a_3|^2)\right]^6 + [\sigma_b|a_5 - a_6|]^6\right\}^{\frac{1}{6}} - \sigma_{ref} = 0 \tag{3.121}$$

Then, there are seven equations (Eq. (3.61) – Eq. (3.66) and Eq.(3.121)) and seven unknowns which are a_1, a_2, a_3, a_4, a_5, a_6, a_7 which must be solved. This is a nonlinear equation system and it can easily be solved numerically by using Minerr command in Mathcad.

3.4. Forming Limit Diagram

Forming limit diagram shows the strain values which lead to failure. The diagram is used for estimating the onset of failure due to necking and location of possible failure spots according to different loading histories. Forming limit curves are generally used for tool manufacturing and optimization of stamping tools. A schematic view for forming limit diagram is given in Figure 3.1.

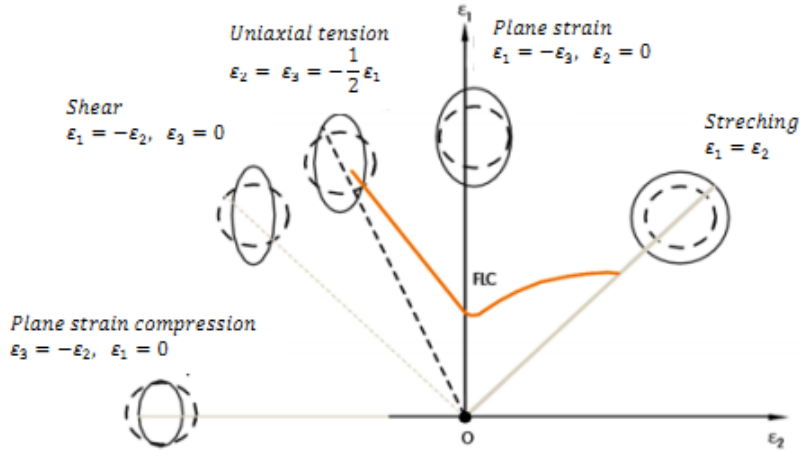

Figure 3.1 Forming limit diagram [8]

The axes of the forming limit diagram represent the major and minor principal strains. The points on forming limit curve correspond the failure strains. The curve represents the boundary for failure of corresponding specimen. Forming limit curve is plotted according to different strain ratios, from pure shear to equibiaxial tension. Positive strain ratios where minor strains are positive correspond the stretching and negative strain ratios where minor strains are negative correspond tension, compression and shear loadings. Forming limit diagram is dependent on strain path and is not successful to represent the failure behavior of the materials which have nonlinear strain path.

For determining forming limit diagram, experimental methods are generally used. However, they require complex experimental set-up and experimental procedure. Due to this complexity on experimentation, some theoretical models were introduced on the basis of the classical or modified Swift and Hill instability criteria [51–53]. Also for recent years, forming limit diagram determination procedure is done numerically by finite element method.

3.4.1. Experimental Forming Limit Diagrams

The most popular way of determining forming limit diagram of materials is the experimental method. Nakazima test is one of the most widely used experimental procedures. This test is performed by deforming sheet metal blank geometries using a hemispherical punch to the fracture of the cup. Different loading conditions are represented by various width and blank geometry.

For performing experimental work, a pattern of small circles is formed on the specimen before deformation. When the sheet is deformed, the circles are deformed into ellipses. Then, the deformed circular patterns are measured using magnifying glasses or microscopes. Recently, there are some optical measurement tools for Nakazima test which makes experimental work easy and accurate. The equipment for Nakazima test consists of a hemispherical punch, a die with the draw bead, blank holder and optical measuring tool.

Figure 3.2 Example of blank specimens for Nakazima test [8]

3.4.2. Numerical Forming Limit Diagrams

Although experimental methods are the most reliable forming limit diagram determination technique, it necessitates also a complex experimental setup and time-consuming experimental effort. Numerical methods are relatively newly developed for determination of forming limit diagrams of materials and performed with commercial finite element simulations tools. They are mainly based on the simulation of Nakazima or other formability tests using finite element analysis tools. In order to predict fracture in corresponding material, strain localization criteria or ductile damage models must be used. For most finite element software, there is no implemented strain localization criterion or ductile failure criteria.

One of the mostly used criterion for strain localization is maximum strain acceleration criterion [46,54–58]. This is based on the evaluation of second time derivative of major strain with respect to time. In this criterion, after maximum strain acceleration is attained, the localized thinning proceeds gradually until the onset of fracture [47]. An example for strain acceleration method is in Figure 3.3.

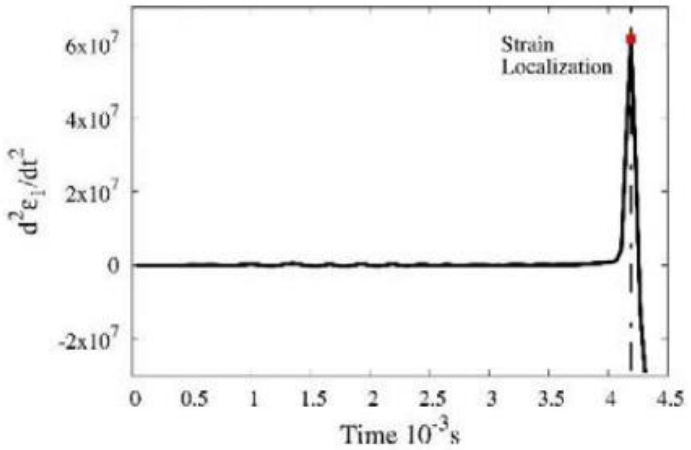

Figure 3.3 Prediction of failure time by strain acceleration criteria [56]

Another strain localization criterion for determining failure time is the ratio of equivalent plastic strain increment [47]. The ratio of equivalent plastic strain increment is calculated by using the critical and adjacent element. The critical element is characterized by Nakazima test and is generally located in the center of the specimen and the adjacent element is located five elements away from the critical element along the rolling direction [47]. If corresponding ratio is larger than 10, it is observed as the localized necking [47]. An example for the ratio of equivalent strain increment is given in Figure 3.4.

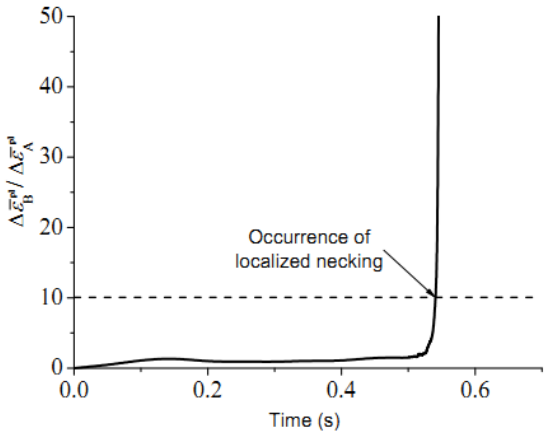

Figure 3.4 Failure time prediction by the ratio of equivalent strain increment [47]

Another strain localization criterion is maximum punch force criterion. After punch force with respect to punch stroke reaches maximum, localized thinning is assumed to be observed. An example for the maximum punch force criterion is given in Figure 3.5.

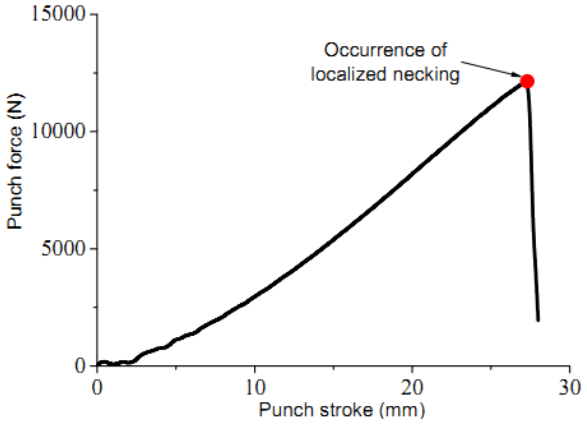

Figure 3.5 Prediction of failure by the maximum punch force criterion [47]

For determining forming diagram, maximum strain acceleration criterion is used in this study for strain localization according to the results obtained from [47]. It is assumed that necking occurs after maximum strain acceleration is reached and failure strains are determined at the next time step. In application of maximum strain acceleration criterion, plastic equivalent strain vs. time data is obtained for the most critical element according to finite element analysis results. Then, the second derivative of this tabulated data is taken by using forward difference method with 4 points whose formulation is given in as:

$$f''(x) = \frac{-f(x+3\Delta t) + 4f(x+2\Delta t) - 5f(x+\Delta t) + 2f(x)}{\Delta t^2} \qquad (3.122)$$

where x is function variable and Δt is the step time. As the examples for maximum strain acceleration criterion, strain acceleration vs. time data of DKP steel for quasi-static case with blanks having 50 mm, 75 mm and 125 mm width are given in Figure 3.7, Figure 3.7 and Figure 3.8. For all three specimens, there is a global maximum of strain acceleration and after that point necking is assumed to start.

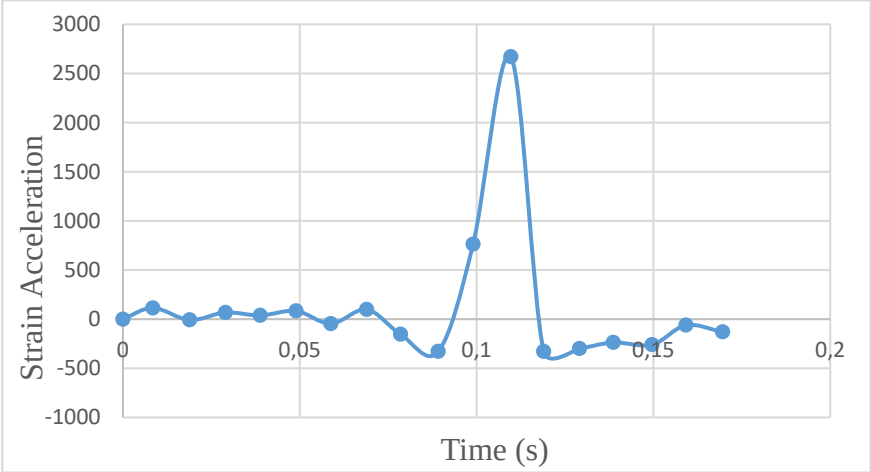

Figure 3.6 Strain acceleration vs. time for 50 mm-width DKP6112 specimen quasi-static case

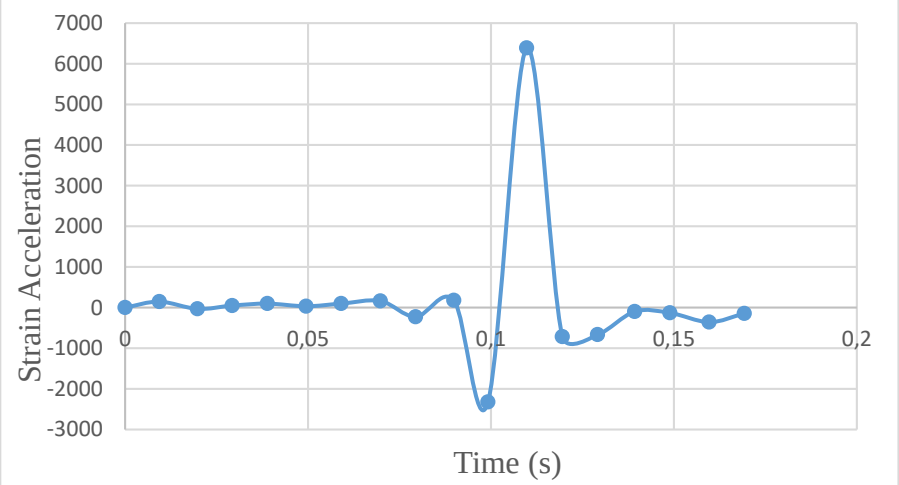

Figure 3.7 Strain acceleration vs. time for 75 mm-width DKP6112 specimen quasi-static case

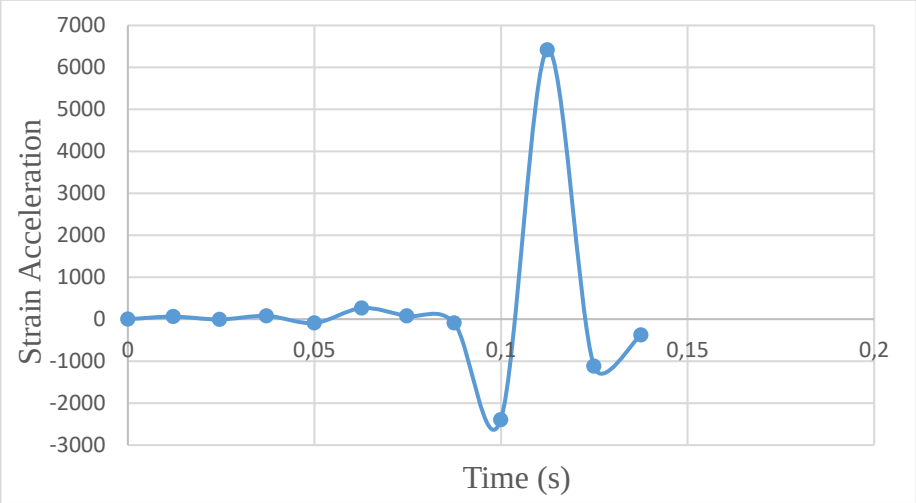

Figure 3.8 Strain acceleration vs. time for 125 mm-width DKP6112 specimen quasi-static case

CHAPTER 4

FINITE ELEMENT MODEL

In finite element analyses, there are basically two solution methodologies; implicit and explicit integration methods. Implicit integration is the method that calculates the residual forces at each step and continues until residual forces being decreased to a specific tolerance which satisfies the convergence criteria. Tangential stiffness methods and Newton-Raphson method are used for implicit method [34]. For explicit method, displacements are calculated from the values at the beginning of the increment. There is no need to calculate stiffness matrices. Generally, backward Euler method is used for explicit integration scheme [8]. For quasi-static analysis, it can be concluded that implicit method gives more accurate results than dynamic explicit method. However, implicit method uses integration time steps considerably greater than dynamic explicit method [34]. In dynamic explicit integration method, a single equation is used to evaluate new nodal variable for a single time step. An implicit solution contains information obtained from solving simultaneous equations for the full grid for each time step. As a result, computational cost of explicit method is significantly lower than implicit method. For explicit method, computational cost increases linearly with the size of the problem, while it increases more rapidly for implicit method [34]. It can be concluded that explicit method is suitable for large and complex contact problems, whereas implicit method is suitable for problems that have relatively smaller domain. The simulation of large problems in real time is a costly process in finite element analysis. To overcome that, two solutions are proposed which are changing loading rate and changing the density of material [34]. First alternative is not suitable for dynamic analysis since strain rate is changed. The second alternative which is called mass scaling is preferable. In this method, density of the material is increased artificially by a factor. Runtime is improved by the square root of

corresponding factor [34]. Mass-scaling scheme is a powerful and preferred method to speed up analyses, however mass-scaling factors must be kept in reasonable values to obtain realistic results [34]. In this study, explicit method is applied by using ABAQUS software.

In the current study, elastic predictor-plastic corrector method is used for all VUMAT subroutines which are used to operate some yield criterion in ABAQUS. According to method, the deformation is assumed to be purely elastic first and incremental change of stress is calculated. In Figure 4.1, elastic predictor-plastic corrector scheme is shown for Von-Mises yield criterion.

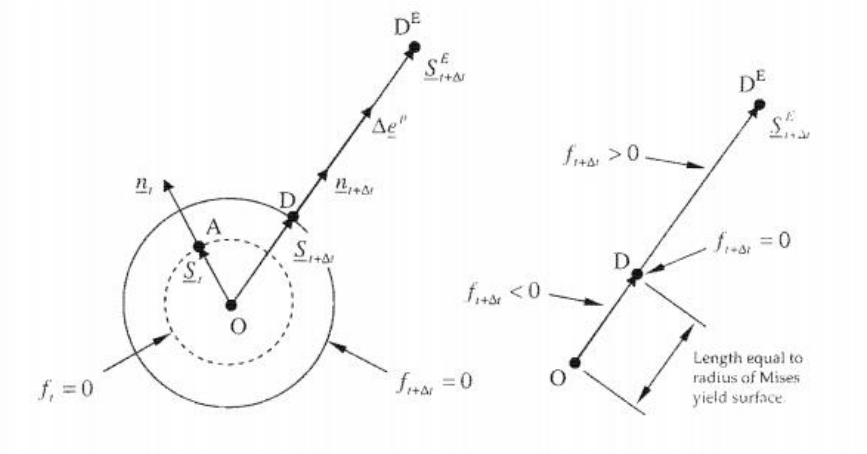

Figure 4.1 Elastic predictor-plastic corrector scheme [59]

In the figure, yield function is represented with f and the unit normal of yield surface is represented with *n*. As it can be observed from Figure 4.1, a trial stress which is shown by point D^E according to Hooke's Law value is calculated first. Corresponding equivalent stress is compared with yield stress calculated from constitutive model that is used in calculation scheme [59]. According to the sign of the difference of these values, it can be determined that the case is elastic or plastic. If equivalent stress is

greater than calculated yield stress value from corresponding constitutive relation, then the stress state is returned to a point which is located on the yield surface [59]. For von Mises yield criterion, the return is performed in radial direction which is perpendicular to corresponding yield surface based on normality rule. The directionality is dictated by the associated flow rule. If any other yield criterion is desired to be used, yield surface and return algorithm must be updated according to corresponding yield criterion.

In this study, VUMAT subroutine is used for dynamic explicit analyses to define the material behavior with different yield criterion. Calculations are done according to current increment. Organizational chart of a typical VUMAT subroutine is given in Figure 4.2. All of these steps are included in built VUMAT subroutine.

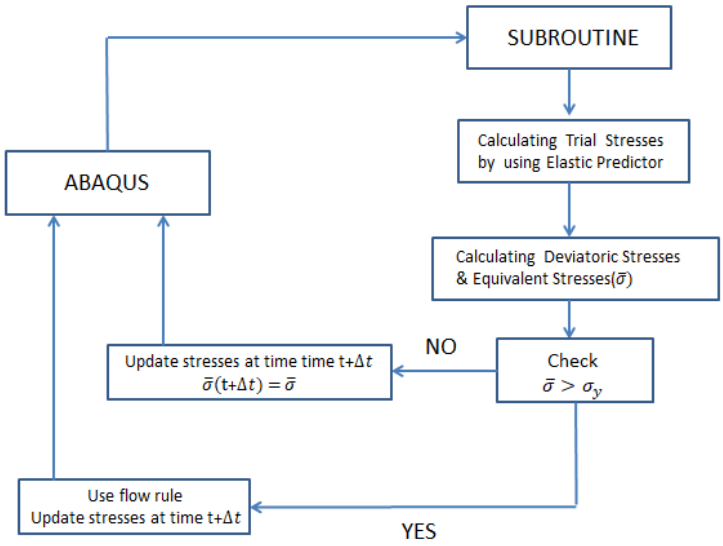

Figure 4.2 VUMAT subroutine process flowchart

User subroutine codes are written by using Fortran programming language. To execute the user subroutine, ABAQUS, Fortran compiler and Microsoft Visual Studio must be linked with the versions of corresponding tools compatible with each other. For this purpose, ABAQUS 6.14-1, Intel Parallel Studio XE 2013 and Microsoft Visual Studio 2012 are used in this study.

4.1. Deep Drawing Die Geometries

Three different punch configurations, which are hemispherical, cylindrical flat and square, are used in analyses. The visual representation of the different punches used is given in Figure 4.3.

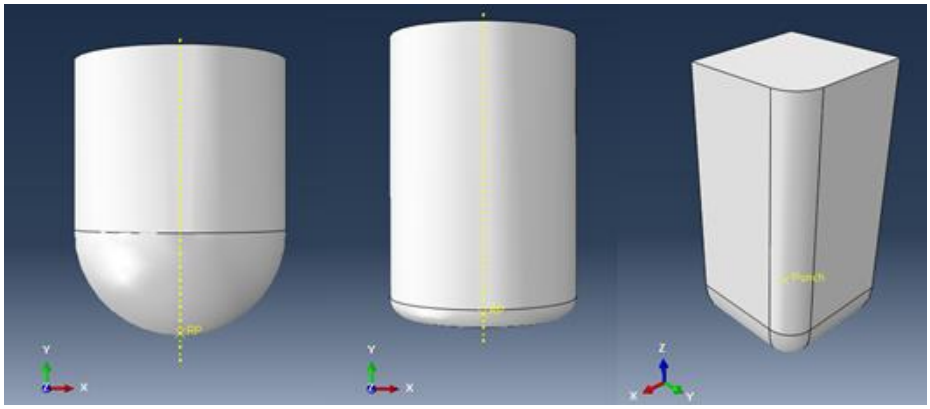

a) b) c)

Figure 4.3 Configurations used for a) hemispherical b) cylindrical c) square punches

In the mesh of blanks there are 762 S4R elements for hemispherical punch and die set, 764 S4R elements for cylindrical flat punch and die set and 650 S4R elements for square punch and die set. In all of the analyses, the die, blank holder and punch are modelled as rigid. For all of the blanks used in analyses the quarter of actual blank are modelled in order to decrease the computational cost. The dimensions of punch die

and blank for three deep drawing processes are given in the following table. All of the punch configurations used in analyses are shown in Figure 4.4.

Table 4.1 Dimensions for used for the three deep drawing operations [4]

Hemispherical Punch	**Cylindrical Punch**	**Square Punch**
Blank Diameter : 110 mm	Blank Diameter : 110 mm	Blank : 80x80 mm
Punch Diameter : 50 mm	Punch Diameter : 50 mm	Punch : 40x40 mm
Die Outer Dia. : 115 mm	Die Outer Dia. : 115 mm	Punch/Corner Rad. : 10/4.5
Die Inner Dia. : 53 mm	Die Inner Dia. : 53 mm	Die Inner Dim. : 42x42
Die Shoul. Rad. : 13.5 mm	Die Shoul. Rad. : 13.5 mm	Die Shoul. Rad. : 13.5 mm

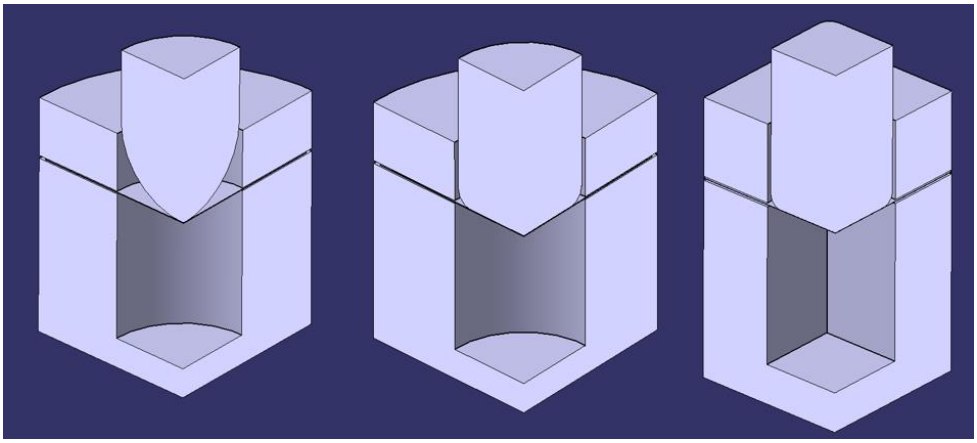

a) b) c)

Figure 4.4 Configurations for a) hemispherical b) cylindrical c) square die sets

4.2. Finite Element Simulation of Nakazima Test for Determining Forming Limit Diagram

4.2.1. Model Parameters

The numerical determination of forming limit diagram is performed by finite element simulation of Nakazima Test. Nakazima test requires a hemispherical punch and corresponding die used in FEA. Generally, for Nakazima test, drawbeads are used to avoid undesired material flow. A 5 mm-groove is applied to the die geometry for this purpose. The dimensions of the related equipment are given in *Table 4.2*.

Table 4.2 Dimensions used in the Nakazima test equipment

Nakazima Test Setup
Die & Holder Outer Diameter : 200 mm
Die & Holder Inner Diameter : 200 mm
Die Corner Radius : 10 mm
Punch Radius : 50 mm

For determining forming limit diagram with Nakazima test, a number of specimens with different geometries were used in order to express different kinds of loading. In this study, 8 different specimens were used that can be seen from Figure 4.5 [45]. Blank was modelled with S4R shell elements with reduced integration. Friction coefficient was taken as 0.1 in all simulations. The optimum size of elements was selected as 2 mm according to mesh sensitivity and computational time

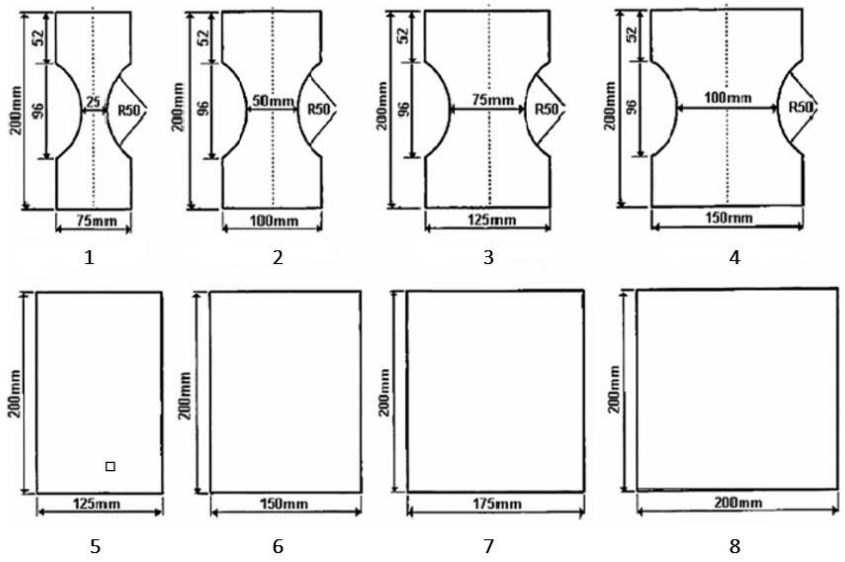

Figure 4.5 Nakazima test blank specimen geometries [45]

CHAPTER 5

MATERIAL DATA

In this study, mild steel DKP6112 and magnesium-aluminum alloy AZ31 are used as the materials in the analyses. The stress-strain curve of DKP6112 and AZ31 material for different temperature and strain rate conditions were obtained from the experimental work of different studies in literature.

5.1. DKP6112 Material

True stress-true strain curves for DKP6112 material for rolling (0°), transverse (90°) and diagonal (45°) directions at quasi-static conditions that were obtained from literature are given in Figure 5.1 [4].

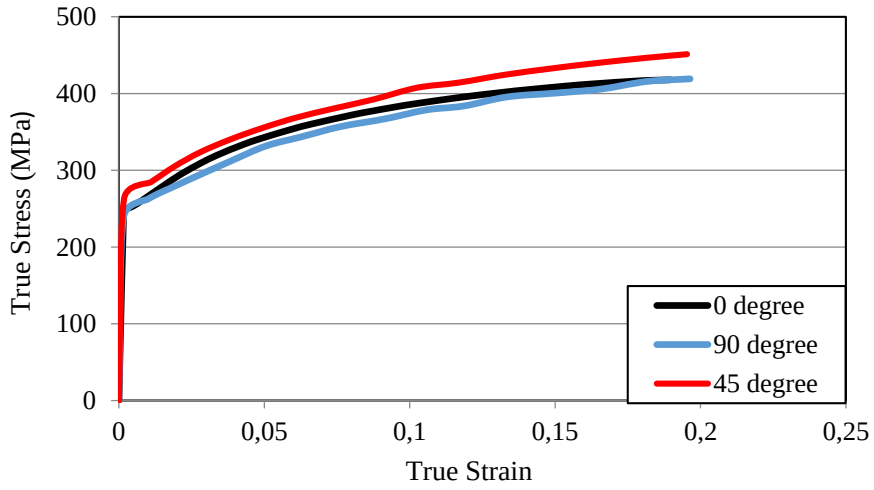

Figure 5.1 True stress vs. true strain data of DKP6112 for quasi-static analyses for different material orientations [4]

For different strain rates, true stress-true strain curves is given in Figure 5.2 that are built by the strain rate sensitivity data determined from.

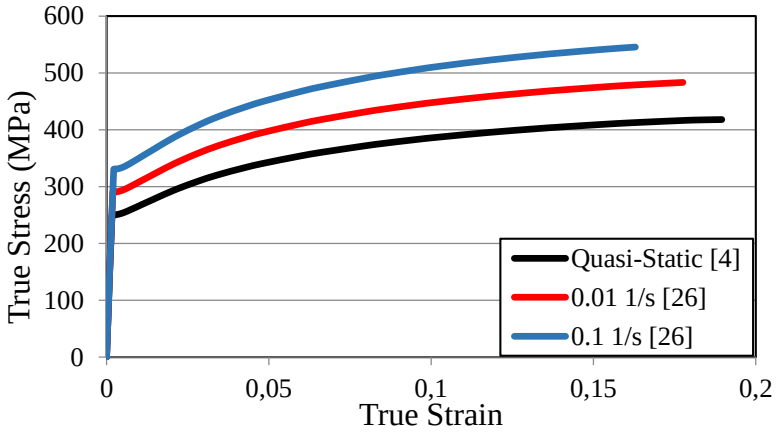

Figure 5.2 True stress vs. true strain data of DKP6112 for different strain rates

5.2. AZ31 Material

For AZ31 material, quasi-static and dynamic true stress-true strain curves were obtained from the experimental work given in [40].

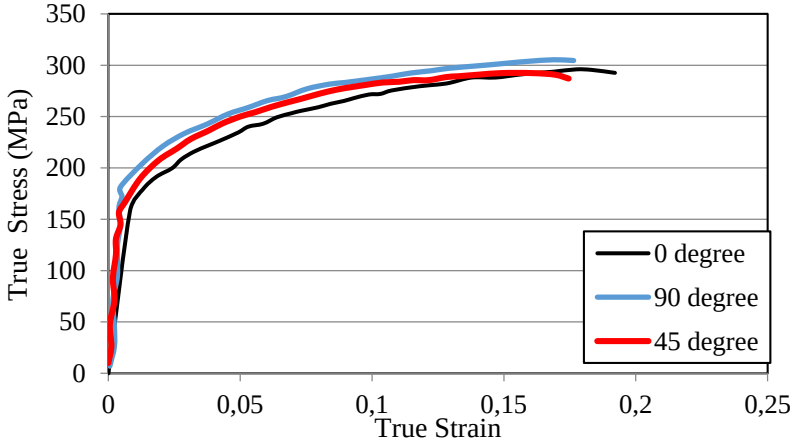

Figure 5.3 True stress vs. true strain data of AZ31 for quasi-static analyses [40]

In Figure 5.3, quasi-static true stress-true strain curves for different material orientations are given. In Figure 5.4, stress-strain curves for different strain rate and temperature values are presented. For quasi-static case, strain rate is taken as 10^{-4} s^{-1}.

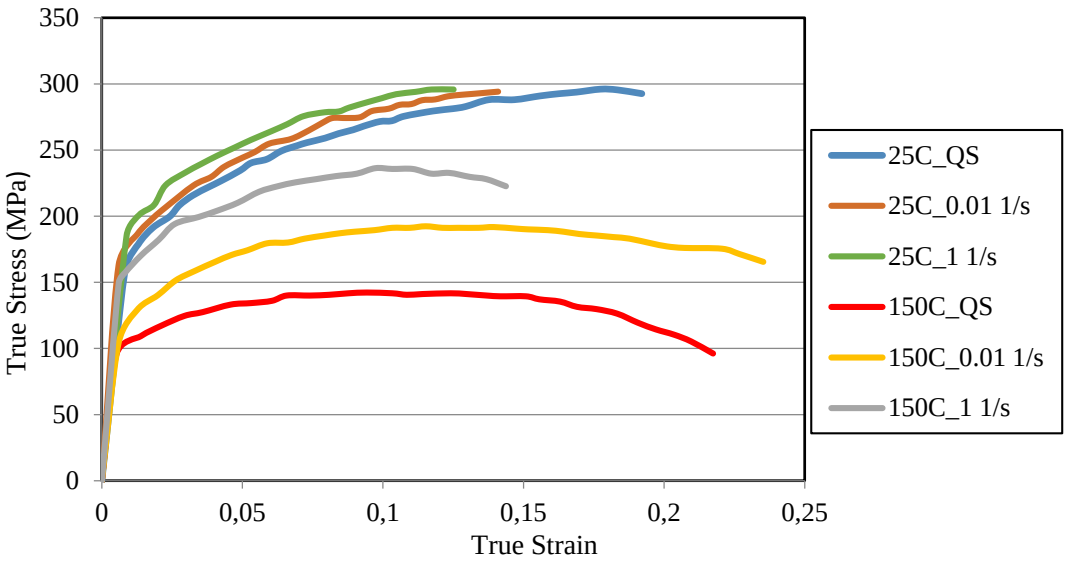

Figure 5.4 True stress vs. true strain data of AZ31 for different strain rate and temperatures [40]

5.3. Material Constants for Different Phenomenological Stress-strain Relations

Table 5.1 Material constants of DKP6112 material for different strain-rate-dependent model

Model	Strain-Dependent Part			Strain-Rate Dependent Part
	A	B	n	
Johnson-Cook	249	526.2	0.6194	C = 0.069
Rule-Jones	249	526.2	0.6194	C = 0.0653
Couque	249	526.2	0.6194	C = 0.0692 D = 0.01 k = 0.0008
Tuazon	249	526.2	0.6194	C = 0.2171 P = 0.3

From the data presented in Section 5.1, material constants for Johnson-Cook, Rule-Jones, Couque and Tuazon models are determined. Material constants for DKP6112 and AZ31 materials are presented in *Table 5.1* and *Table 5.2*.

Table 5.2 Material constants of AZ31 material for different strain-rate-dependent model

	Strain-Dependent Part			**Strain-Rate Dependent Part**	**Temperature-Dependent Part**
	A	**B**	**n**		**m**
Johnson-Cook	151	306.7	0.4069	C = 0.0093	0.4853
Rule-Jones	151	306.7	0.4069	C = 0.0371	0.4853
Couque	151	306.7	0.4069	C = 0.0044 D = 0.0299 k = -0.0589	0.4853
Tuazon	151	306.7	0.4069	C = 0.0775 P = 0.0463	0.4853

5.4. Material Constants for Yld2003-8p Yield Criteria

For dynamic cases, yield stress values are taken from quasi-static experimental data [40] by using Johnson-Cook model. It is assumed that anisotropy coefficients for different directions are the same for all strain rate configurations since the strain rate multiplier coming from Johnson-Cook model is accepted as the same for all directions. In *Table 5.3*, material properties of DKP6112 obtained from uniaxial tension and equibiaxial tests are given for different strain rate conditions. Material properties of AZ31 alloy are given in the following figures for different temperatures by using the same assumptions and stress prediction methodology applied for the case of DKP6112 material.

Table 5.3 DKP6112 material properties from uniaxial tension and equibiaxial test at room temperature

	σ_0	σ_{45}	σ_{90}	σ_b	r_0	r_{45}	r_{90}
Quasi-Static [4]	250	256	242	281	1.34	0.99	1.67
0.01 (1/s)	330.6	338.5	320	371.6	1.34	0.99	1.67
1 (1/s)	411.2	421	398	462.2	1.34	0.99	1.67

Table 5.4 AZ31 material properties from uniaxial tension and equibiaxial test at room temperature [40]

	σ_0	σ_{45}	σ_{90}	σ_b	r_0	r_{45}	r_{90}
Quasi-Static	158.3	161.5	164	190	1.25	0.86	0.69
0.01 (1/s)	165	168.4	171	198	1.25	0.86	0.69
1 (1/s)	171.8	175.3	178	206.3	1.25	0.86	0.69

Table 5.5 AZ31 material properties from uniaxial tension and equibiaxial test at 150°C [40]

	σ_0	σ_{45}	σ_{90}	σ_b	r_0	r_{45}	r_{90}
Quasi-Static	95.5	89.5	92	99.4	1.25	0.86	0.69
0.01 (1/s)	99.6	93.3	96	103.7	1.25	0.86	0.69
1 (1/s)	103.7	97.2	99.9	107.9	1.25	0.86	0.69

CHAPTER 6

RESULTS & CONCLUSION

6.1. Verification of Numerical Models Using Quasi-static Cases

Results of finite element analyses of forming with hemispherical, cylindrical and square punches have been verified by quasi-static cases for DKP6112 steel material. Experimental thickness strain values are taken from [4]. Von Mises yield criterion was used with isotropic, kinematic and combined hardening models. Hill48 and Yld2003 yield criteria were used with isotropic hardening model. For Yld2003 analyses, VUMAT subroutines were used. For other yield criteria, built-in features of ABAQUS were used. Finite element models give reasonably close results to experimental findings. Then, it was decided that the finite element model is verified and analyses were applied for different strain rate and temperature conditions with the same finite element model.

6.1.1. Forming with Hemispherical Punch

For hemispherical punch/die set, 20 mm, 35 mm and 45 mm punch travel values are used for analyses. For 20 mm punch travel, results of Yld2003 yield criterion agree well with cup bottom and flange area. According to Figure 6.1, for cup wall and flange region, results are deviating from experimental results for von Mises yield criterion with isotropic hardening, von Mises yield criterion with kinematic hardening, von Mises yield criteria with combined hardening and Hill48 models which are the similar cases resulted in [4]. Especially for the cup flange region, none of the models except Yld2003 can model the material flow correctly. For 20 mm punch travel, the results of Hill 48 model and von Mises models are close to each other.

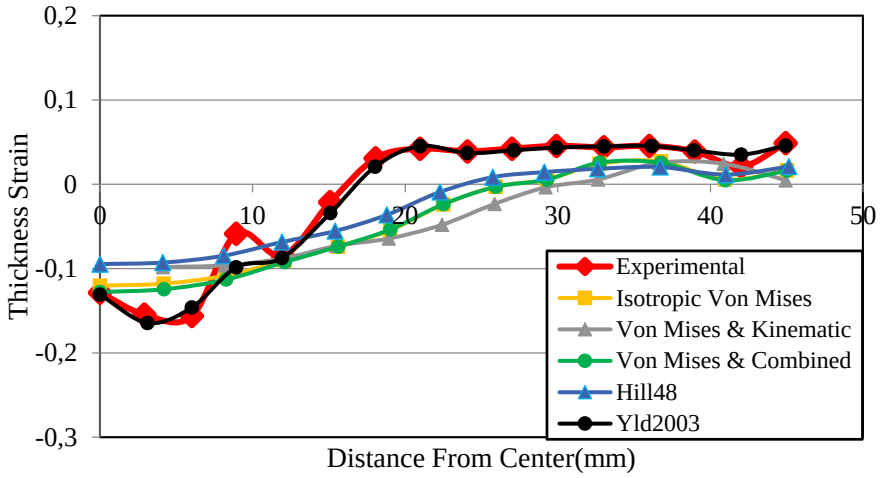

Figure 6.1 Thickness strain distribution of the cup for yield criteria and hardening models at 20 mm punch travel

Thickness strain distribution for 35 mm punch travel is given in *Figure 6.2*. For 35 mm punch travel, different models give closer results to experimental one with respect to 20 mm punch.

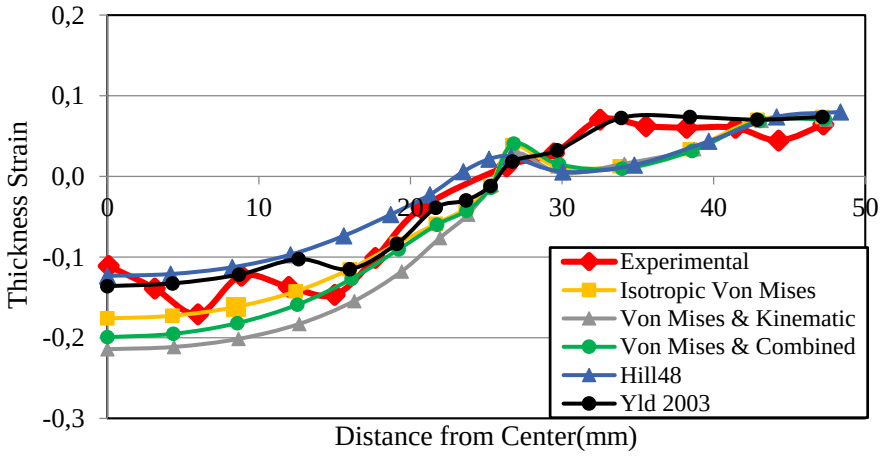

Figure 6.2 Thickness strain distribution for different yield criteria and hardening models at 35 mm punch travel

Hill48 and Yld2003 models give close results to experimental results for the region under the punch and cup wall region and there is a distinguishable difference from von Mises models. Accordingly, it can be commented that significance of anisotropy increase with increasing punch travel. For flange region, only Yld2003 model agrees well with experimental results. In this region, Hill48 is not successful to model the thickness strain distribution especially for the die corner**.** Thickness strain distribution with different yield criteria and hardening models for 45 mm punch travel are given in *Figure 6.3*. Yld2003 model agrees well with experimental results for all cup area. Isotropic, combined hardening models with Von Mises and Hill48 models have relatively minor deviations from experimental results. For the region under the punch, Hill48 model give good results also. For cup wall and cup flange regions, isotropic and combined hardening model with Von Mises give close results to experimental results.

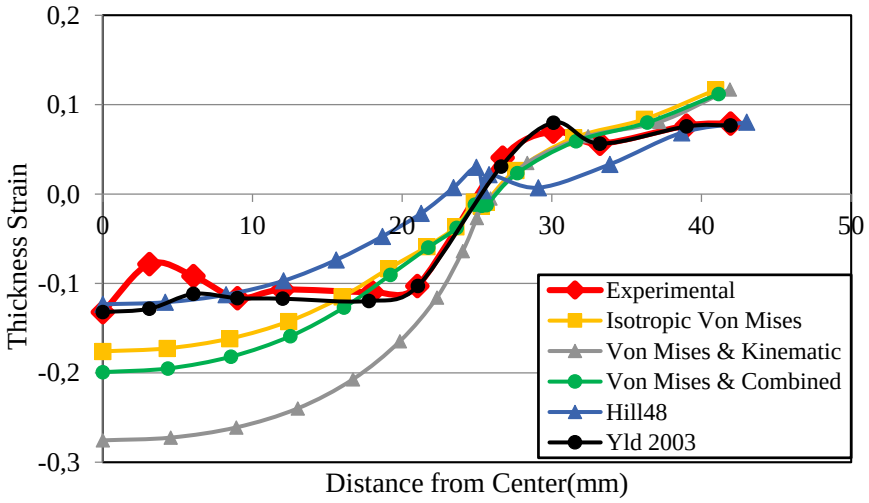

Figure 6.3 Thickness strain distribution for different yield criteria and hardening models at 45 mm punch travel

6.1.2. Forming with Cylindrical Flat Punch

Thickness strain distributions of cylindrical flat punch with 15 mm and 25 mm punch travel are given in *Figure 6.4* and *Figure 6.5*. For 15 mm punch travel, Yld2003, Hill48 and von Mises models with different hardenings have close results to experimental one except the critical thinning region. Yld2003 model gives close results in critical thinning region for 15 mm punch travel. For flange region, also all models give good results, but the best model for this region is also Yld2003.

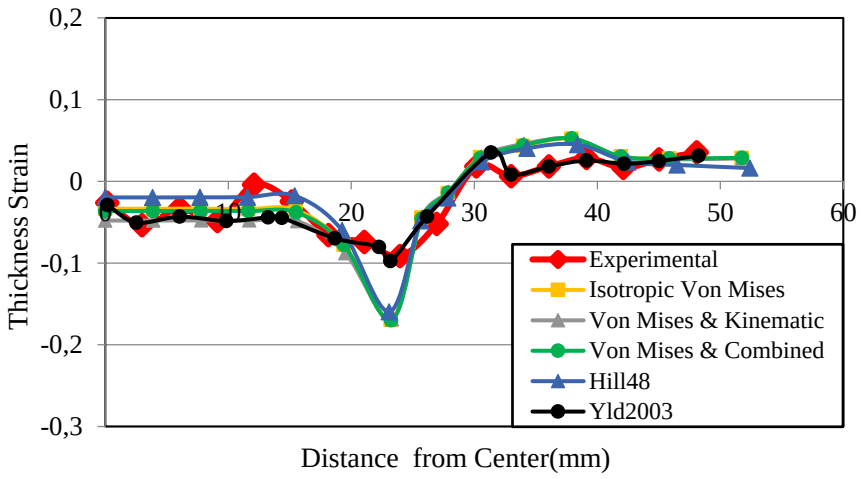

Figure 6.4 Thickness strain distribution for different yield criteria and hardening models at 15 mm punch travel

For 25 mm, all of the models give close results to experimental one in cup flange region. For cup bottom region, von Mises yield criteria with kinematic hardening model shows significant deviation from experimental results. For critical thinning region, Yld2003 yield criteria gives the best results.

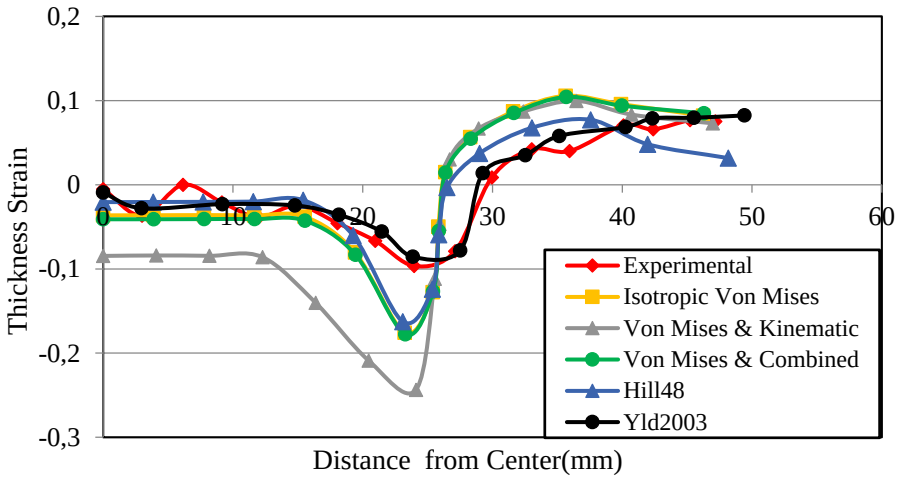

Figure 6.5 Thickness strain distribution for different yield criteria and hardening models at 25 mm punch travel

6.1.3. Forming with Square Punch

Thickness strain distributions of square punch with 15 mm and 20 mm punch travel are given in *Figure 6.6* and *Figure 6.7*.

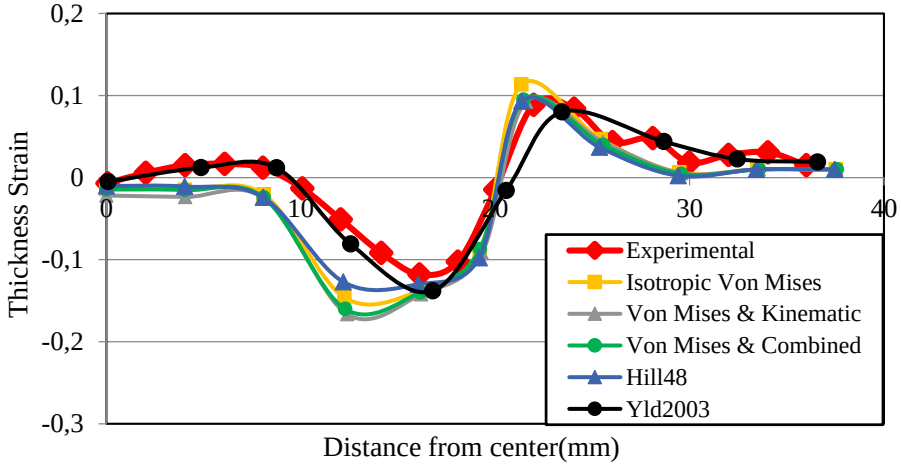

Figure 6.6 Thickness strain distribution for different yield criteria and hardening models at 15 mm punch travel

For 15 mm punch travel, Yld2003 model agrees well with experimental results. For Hill48 and von Mises models, there are minor deviations from experimental results in the region under the punch. For cup wall and flange region, all models give good results according to experimental results.

For 20 mm punch travel, Yld2003 model agrees well with experimental results. For Hill48 and von Mises models, results are deviating from the experimental results in critical thinning region. For cup wall and flange region, all of the models give good results.

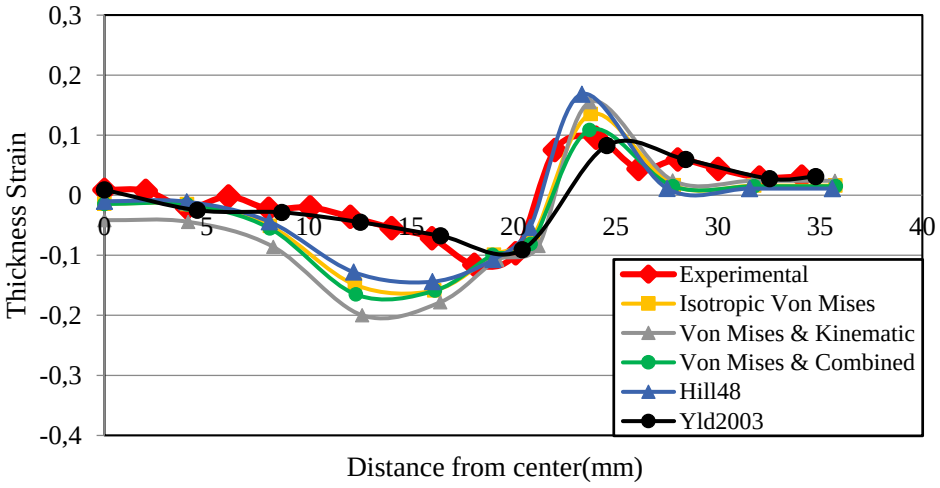

Figure 6.7 Thickness strain distribution for different yield criteria and hardening models at 20 mm punch travel

6.1.4. Discussion for Model Verification with Quasi-static Cases

According to results in Section 6.1.1, 6.1.2 and 6.1.3, the finite element model is verified for quasi-static analysis of forming for all punch geometries. Results from finite element simulations agree well with experimental results especially for

Yld2003. According to these results, finite element models are verified for quasi-static case and the same models are used for different strain rate and temperature conditions.

6.2. Effect of Strain Rate and Temperature with von Mises Yield Criterion

The results have been obtained for AZ31 aluminum-magnesium alloy using hemispherical, cylindrical flat bottom and square punch.

6.2.1. Forming with Hemispherical Punch

Analyses are performed for 20 mm punch travel with hemispherical punch configuration by using von Mises yield criterion. Thickness strain and punch force data are given in *Figure 6.8*, *Figure 6.9* respectively.

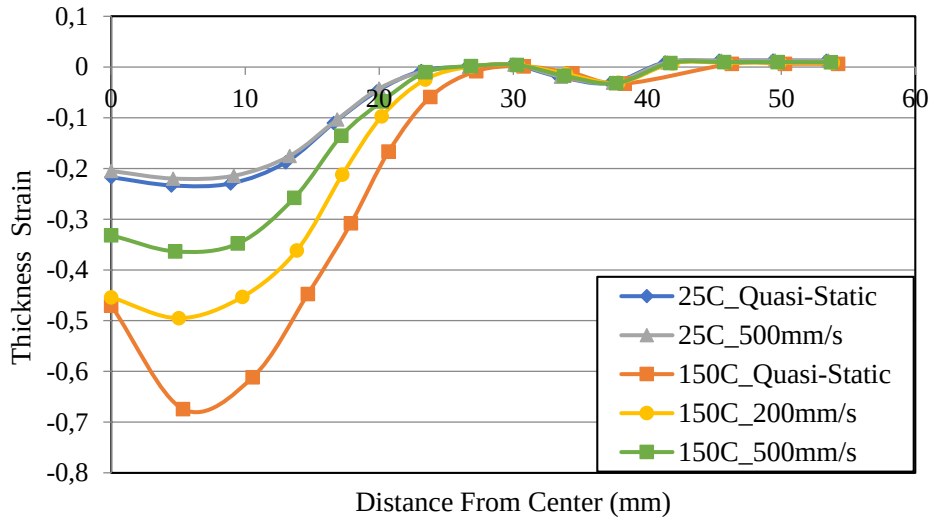

Figure 6.8 Thickness strain vs. distance from center data for different strain rate and temperatures in rolling direction of material

As can be seen from *Figure 6.8*, the magnitude of thickness strain increases with increasing temperature in the cup region since ductility of the material significantly increases. For higher values of strain rate, there is not a significant change for quasi-static case. For higher temperatures, effect of strain rate becomes significant. Punch force vs. punch travel graph is given in *Figure 6.9*. For higher temperatures, the strength of material decreases. According to that, punch force is significantly lower for higher temperatures than room temperature. For higher strain rate values, material is expected to be relatively stronger in the same temperature. As a result, punch force is increased for higher strain rate values.

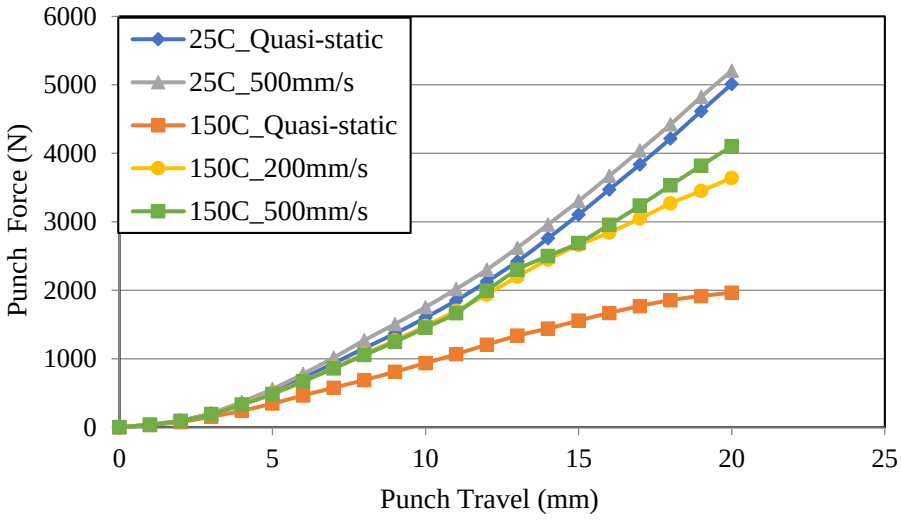

Figure 6.9 Punch force vs. distance from center data for different strain rate and temperatures in rolling direction of material

6.2.2. Forming with Cylindrical Flat Punch

Analyses are performed for 20 mm punch travel with cylindrical flat punch configuration by using von Mises yield criterion. Thickness strain and punch force data are given in *Figure 6.10* and *Figure 6.11*.

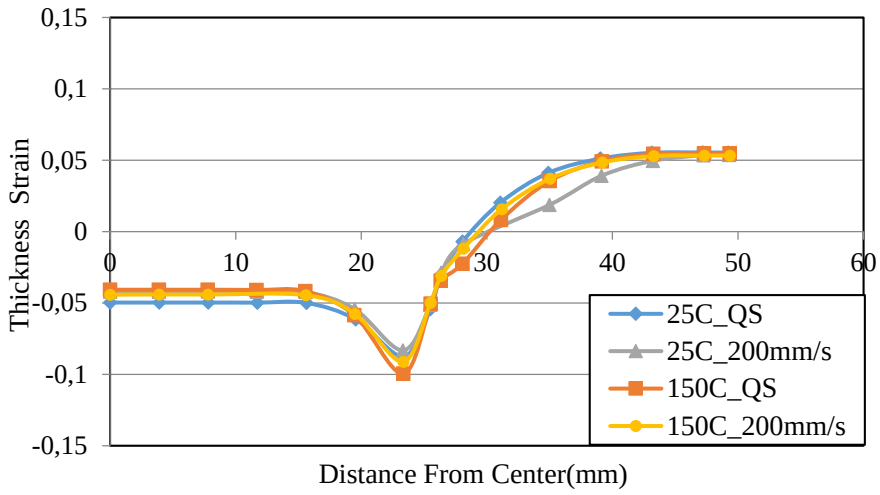

Figure 6.10 Thickness strain vs. distance from center data for different strain rate and temperatures in rolling direction of material

Thickness strain values in the critical thinning region are increasing with increasing temperature and slightly decreasing with increasing strain rate similar to hemispherical punch configuration case.

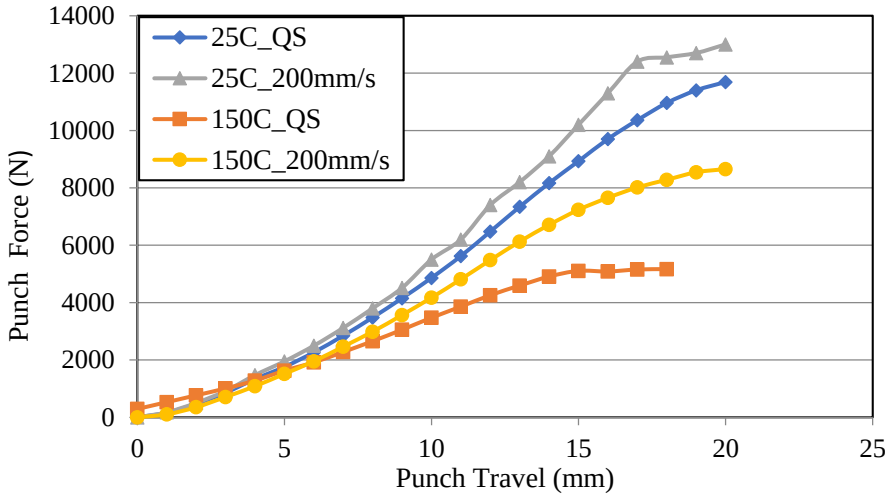

Figure 6.11 Punch force vs. distance from center data for different strain rate and temperatures in rolling direction of material

Punch force values are decreasing with increasing temperature and increasing with increasing strain rate similar to the hemispherical configuration case. According to that, cylindrical cup drawing operation will proceed relatively easier for elevated temperatures. According to the results, thickness strain distributions do not significantly change with different conditions however; this is not the case for the punch force results. Although stress-strain relations are almost the same for different conditions the mechanical properties of the materials varying with strain rate and temperature result in different punch forces.

6.2.3. Forming with Square Punch

Analyses are performed for 20 mm punch travel with square punch by using von Mises yield criterion. Thickness strain and punch force results according to the distance from center are given in *Figure 6.12* and *Figure 6.13*, respectively. Thickness strain values in the critical thinning region are increasing with increasing temperature and decreasing with increasing strain rate similar to hemispherical and cylindrical flat punch case.

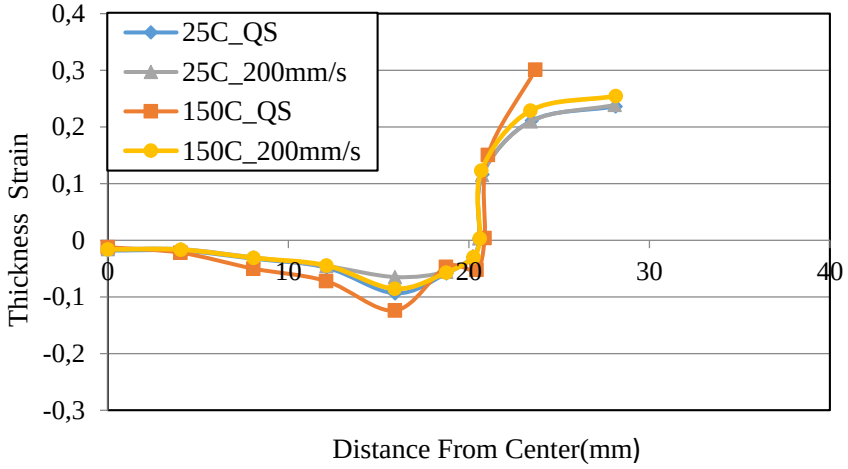

Figure 6.12 Thickness strain vs. distance from center data for different strain rate and temperatures in rolling direction of material

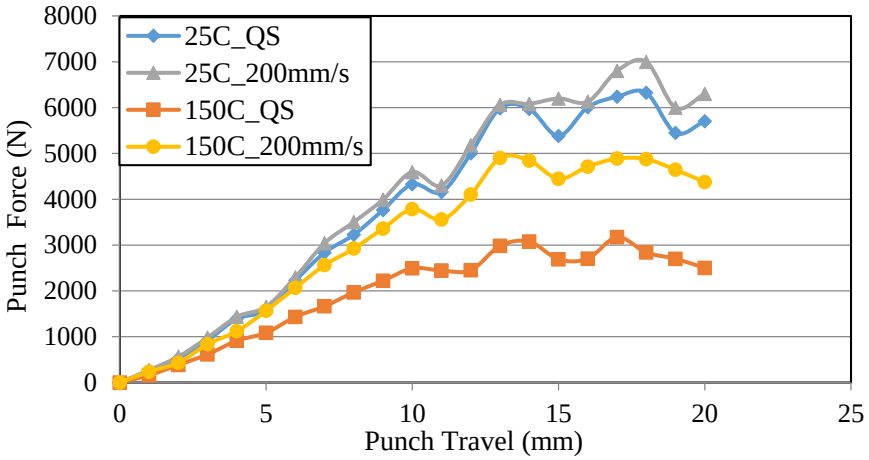

Figure 6.13 Punch force vs. distance from center data for different strain rate and temperatures in rolling direction of material

Punch forces are decreasing with increasing temperature and increasing with increasing strain rate similar to the hemispherical and cylindrical flat punch case. The effect of strain rate on punch force is more pronounced for elevated temperatures. Similar behavior with cylindrical punch in terms of thickness strain distribution and punch forces are observed for this configuration.

6.2.4. Discussion for Effect of Strain Rate and Temperature

According to results, minimum thickness strain decreases with strain rate increase and it increases with temperature increase. Punch force increases with strain rate increase and temperature decrease. These results are valid for all punch geometries. For cylindrical flat bottom and square punches whose minimum thickness regions are concentrated to a relatively sharp corner, thickness strain results are very close to each other for different strain rate and temperatures under the punch compared to hemispherical punch that has smoother geometry. For cylindrical flat bottom and square punches, forming in elevated temperatures is beneficial since critical thinning

is not significantly changing with strain rate and temperature whereas punch force decreases.

6.3. Comparison of the Results for Strain Rate and Temperature-Dependent Phenomenological Stress-strain Relations

In this section, different phenomenological strain-rate-dependent models are compared according to thickness strain for different punch configurations using DKP6112 steel AZ31 aluminum-magnesium alloy material. Analyses are performed for 500 mm/s punch velocity and 25°C temperature.

6.3.1. Hemispherical Punch

For hemispherical punch, thickness strain distributions for DKP6112 are given in *Figure 6.14*.

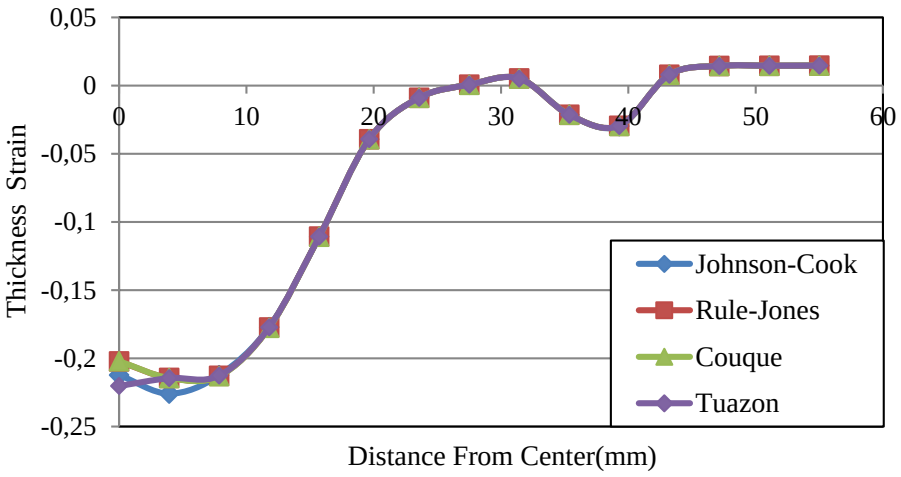

Figure 6.14 Comparison of different models for hemispherical punch using DKP6112 material

Thickness strain distributions for AZ31 are given in *Figure 6.15*. Close results are observed from these four different stress-strain relations for given strain rate and temperature conditions of both material.

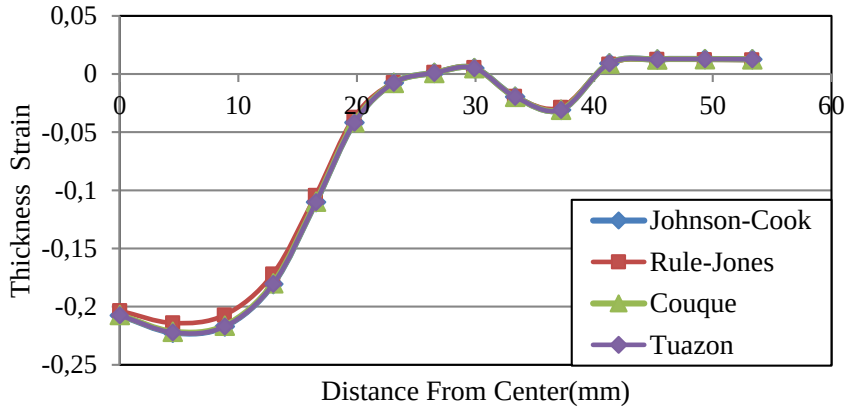

Figure 6.15 Comparison of different models for hemispherical punch using AZ31 material

6.3.2. Cylindrical Flat Bottom Punch

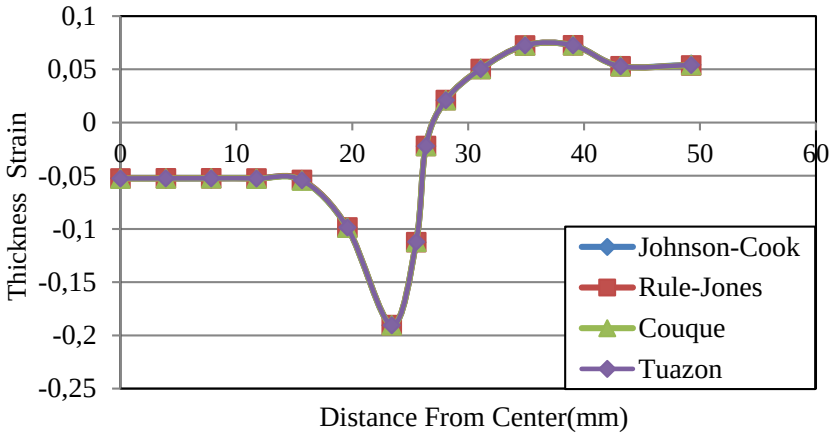

Figure 6.16 Comparison of different models for cylindrical punch using DKP6112 material

For cylindrical punch, thickness strain distributions of DKP6112 are given in *Figure 6.16*.Thickness strain distributions of AZ31 are given in *Figure 6.17*. According to results, thickness strain distributions do not vary with the change of phenomenological stress-strain relation for given strain rate and temperature conditions.

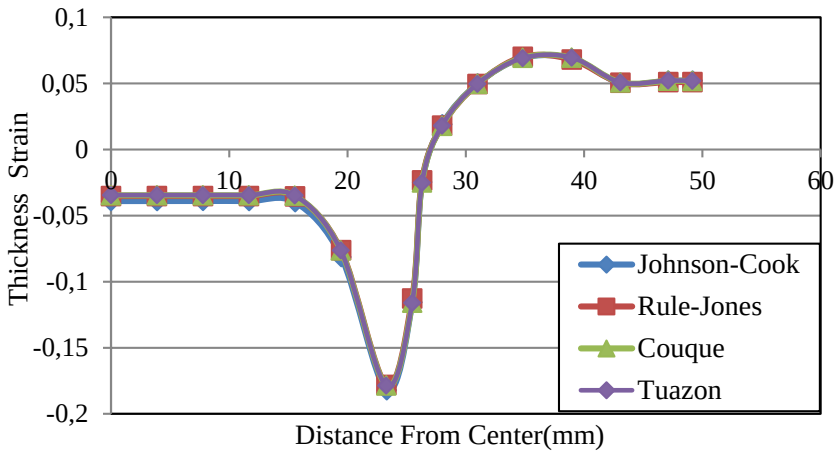

Figure 6.17 Comparison of different models for cylindrical punch using AZ31 material

6.3.3. Square Punch

For square punch, thickness strain distributions of DKP6112 are given in *Figure 6.18*. Thickness strain distributions of AZ31 are given in *Figure 6.19*. Similar to other punch configurations, thickness strain distributions are not changing according to different phenomenological stress-strain relations. In the cup flange region, Johnson-Cook model gives a slight deviation from other models, but it is not a noticeable difference when the whole distribution is considered.

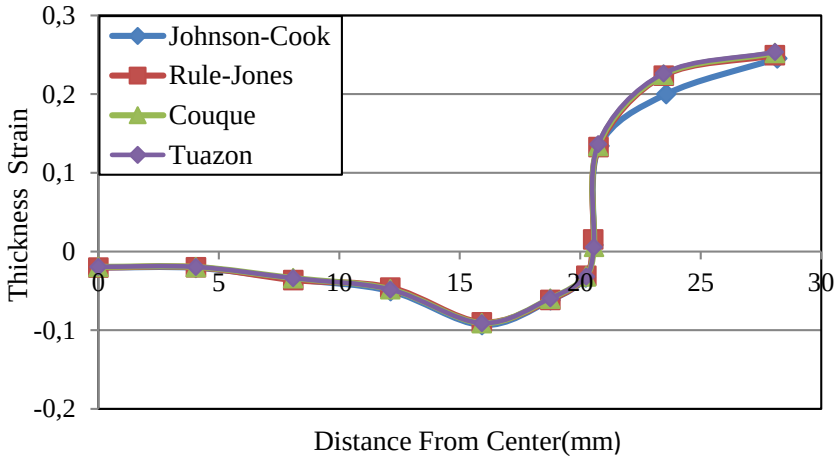

Figure 6.18 Comparison of different models for square punch using DKP6112 material

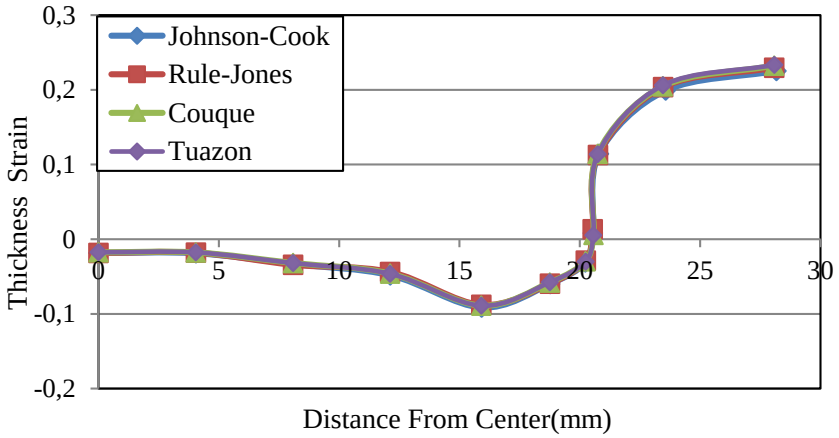

Figure 6.19 Comparison of different models for square punch using AZ31 material

6.3.4. Discussion for Effect of Different Strain Rate and Temperature-Dependent Phenomenological Stress-strain Relations

According to results, it is observed that results for all of the phenomenological stress-strain relations have no significant difference from each other. For strain rate and temperature values suitable for conventional deep drawing, these relations work

similarly. Therefore, for conventional deep drawing analyses, any of these models can be used. It is sensible to choose Johnson-Cook model as the first option because it is relatively easy to implement to the finite element analyses.

6.4. Thickness Strain Results for Different Yield Criteria at Different Strain Rte and Temperature

To observe the effect of yield criteria for different deep drawing configurations, finite element analyses were performed with von Mises, Hill48 and Yld2003-8p yield criteria by using ABAQUS/Explicit. For Von-Mises and Hill48 models, built-in libraries in ABAQUS were used. For Yld2003-8p yield criterion, necessary VUMAT subroutine codes have been prepared by using the constants necessary for Yld2003-8p. To determine the constants, a commercial software was used and the obtained material constants are presented in *Table 6.1* for DKP6112 material. The results presented in *Table 6.2* and *Table 6.3* are for AZ31 material at room temperature and 150°C, respectively. According to these values, the same calculation procedure is done for quasi-static case and seven material constants are determined for all different strain rate and temperature values.

Table 6.1 Seven material constants of DKP6112 for Yld2003 yield criteria at room temperature

	a_1	a_2	a_3	a_4	a_5	a_6	a_7
Quasi-static	1.162	0.727	0.727	0.050	1.080	1.089	0.080
0.01 (1/s)	0.099	0.828	1.726	1.574	1.06	1.077	7.748
1 (1/s)	0.364	0.844	1.622	1.622	1.056	1.179	7.486

Table 6.2 Seven material constants of AZ31 for Yld2003 yield criteria at room temperature

	a_1	a_2	a_3	a_4	a_5	a_6	a_7
Quasi-static	-0.077	0.79	1.737	1.659	1.068	0.949	0.055
0.01 (1/s)	-0.078	0.8	1.73	1.7	1.06	0.95	0.009
1 (1/s)	-0.077	0.79	1.74	1.66	1.068	0.95	0.003

Table 6.3 Seven material constants of AZ31 for Yld2003 yield criteria at 150°C

	a_1	a_2	a_3	a_4	a_5	a_6	a_7
Quasi-static	0.152	0.813	1.817	1.741	1.063	1.039	0.155
0.01 (1/s)	0.043	0.823	1.851	1.79	1.061	1.035	0.096
1 (1/s)	0.015	0.813	1.818	1.74	1.068	1.04	0.132

Thickness strain values with respect to initial blank dimensions were plotted for different punch configurations with different punch velocities and temperatures. Analyses were performed for 20 mm punch travel.

6.4.1. Hemispherical Punch

6.4.1.1. DKP6112 Material

For DKP6112 material at room temperature, the variations thickness strain values with respect to the distance from the center of blank at 200 mm/s punch velocity by using different yield criteria are given in *Figure 6.20*.

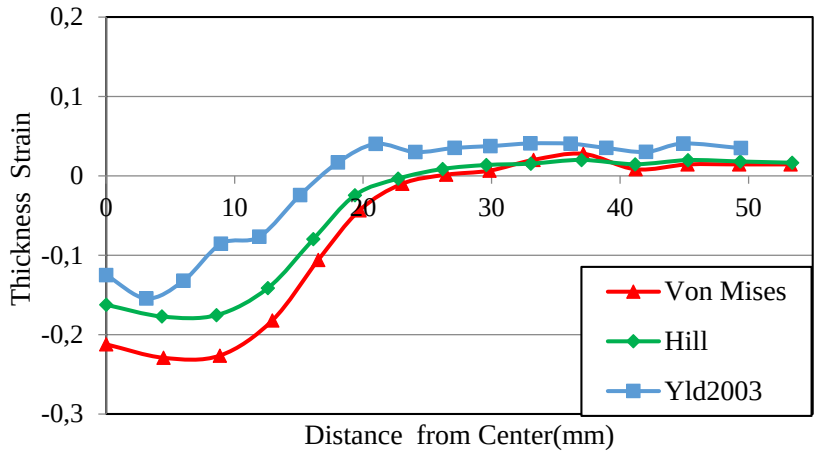

Figure 6.20 Thickness strain distribution for 200 mm/s punch velocity of DKP6112 material for different yield criteria in room temperature

For 200 mm/s punch velocity, similar results are obtained for cup flange region with different models. For this region, greater thickness strain values are obtained with Yld2003 that it gives more reasonable results with respect to the others. In the region below the punch, Yld2003 model estimates relatively lower thickness strain values than Von Mises and Hill48 model.

6.4.1.2. AZ31 Material

For AZ31 in room temperature, the variations of thickness strain values with respect to the distance from the center of blank for 200 mm/s case by using different yield criteria are given in *Figure 6.21*. All models give similar results however, in the region below the punch Yld2003 estimates thickness strain slightly lower than other models. In this case, in cup flange region, von Mises, Hill48 and Yld2003 yield criteria give close results to each other.

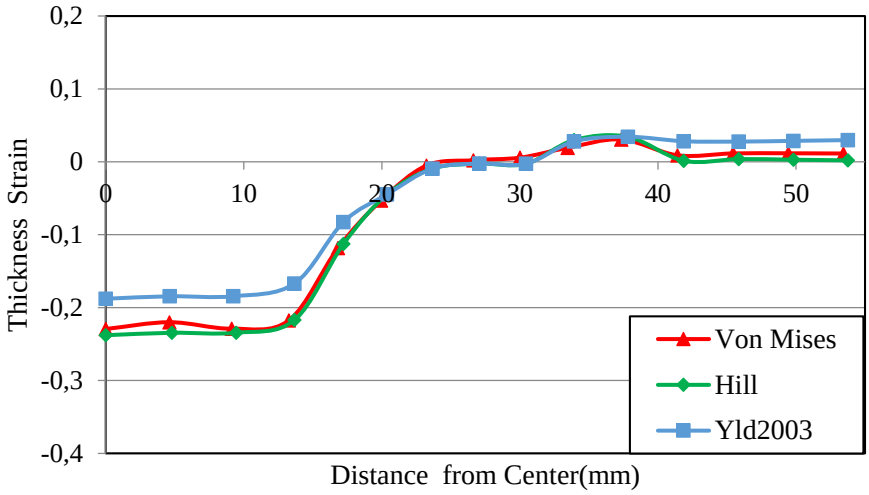

Figure 6.21 Thickness strain distribution for 200 mm/s punch velocity of AZ31 material for different yield criteria in room temperature

For AZ31 in 150°C temperature, the variations of thickness strain values with respect to the distance from the center of blank for quasi-static case by using different yield criteria are given in *Figure 6.22*.

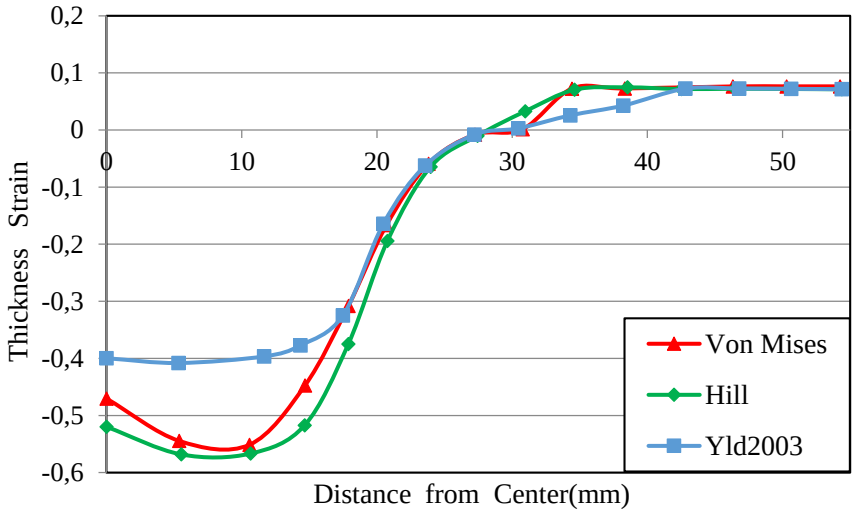

Figure 6.22 Thickness strain distribution for quasi-static case of AZ31 material for different yield criteria in 150°C temperature

With the increase of temperature, the difference between Yld2003 and other models increases. In the region under the punch, von Mises yield criterion differs from Hill48 criterion and gives slightly greater strain values.

For AZ31 material in 150°C temperature, the variations of thickness strain values with respect to the center of blank for 200 mm/s punch velocity by using different yield criteria are given in *Figure 6.23*. For cup wall and flange region, all of the yield criteria give similar thickness strain results. For the region under the punch, anisotropic yield criteria Yld2003 and Hill48 give close results between each other. Von Mises yield criterion estimates thickness strain values for the region under the punch greater than the other yield criteria.

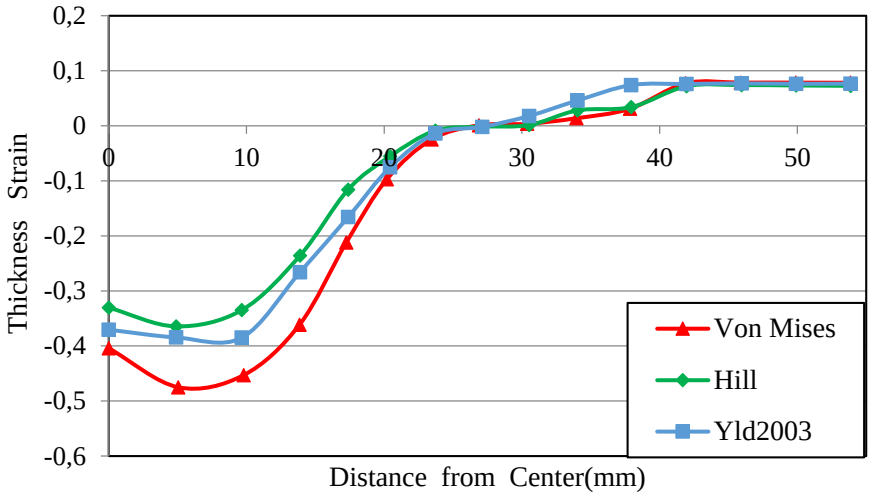

Figure 6.23 Thickness strain distribution for 200 mm/s punch velocity of AZ31 material for different yield criteria in 150°C temperature

6.4.2. Cylindrical Flat Punch

6.4.2.1. DKP6112 Material

For DKP6112 material at room temperature, the variations of thickness strain values with respect to the center of blank for 200 mm/s punch velocity by using different yield criteria are given in *Figure 6.24*. For cup flange region and the region under the punch, von Mises yield criterion estimates greater thickness strain values from the other criteria. In critical thinning section, Yld2003 estimates the thickness strain value significantly lower than other models.

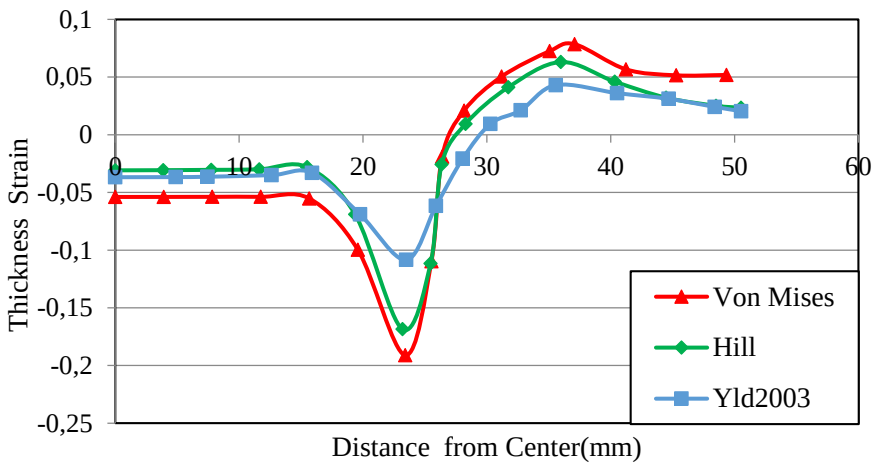

Figure 6.24 Thickness strain distribution for 200 mm/s punch velocity of DKP6112 material for different yield criteria in room temperature

6.4.2.2. AZ31 Material

For AZ31 at room temperature, thickness strain distribution according to the center of blank 200 mm/s case by using different yield criteria are given in *Figure 6.25*. For cup flange and the region under the punch, anisotropic yield criteria estimate thickness strain values greater than von Mises yield criterion. Especially Hill48 yield criterion

estimate thickening effect in cup flange region significantly greater other criteria. In critical thinning section, Yld2003 estimates the thickness strain value significantly lower than other models similar to DKP6112 material.

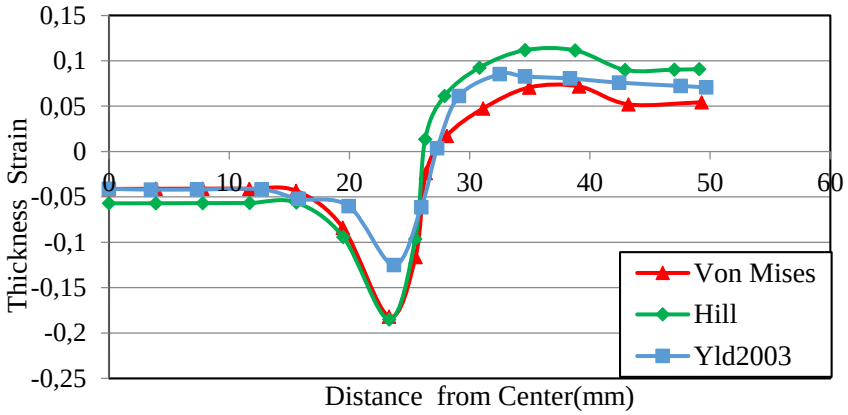

Figure 6.25 Thickness strain distribution for 200 mm/s punch velocity of AZ31 material for different yield criteria in room temperature

For AZ31 material in 150°C temperature, the variations of thickness strain values with respect to the center of blank for quasi-static case by using different yield criteria are given in *Figure 6.26*.

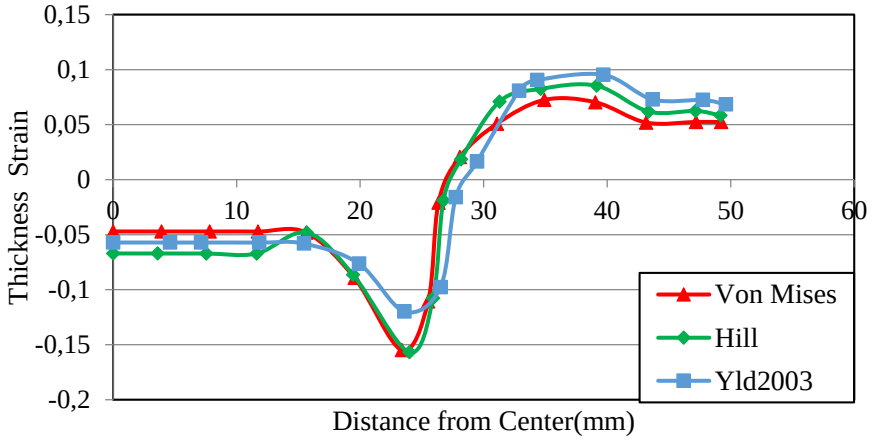

Figure 6.26 Thickness strain distribution for quasi-static case of AZ31 material for different yield criteria in 150°C temperature

Anisotropic yield criteria estimate slightly greater thickness strain values in cup flange region and the region under punch similar to 200 mm/s punch velocity case. In maximum thinning region, Yld2003 gives thickness strain value less than the others.

For AZ31 material at 150°C temperature, thickness strain distribution is given in *Figure 6.27* for 200 mm/s punch velocity by using different yield criteria. For cup wall region, all criteria give close results between each other. For cup flange and the region under the punch, anisotropic yield criteria estimate greater thickness strains. For critical thinning region, Yld2003 gives thickness strain value lower than the others.

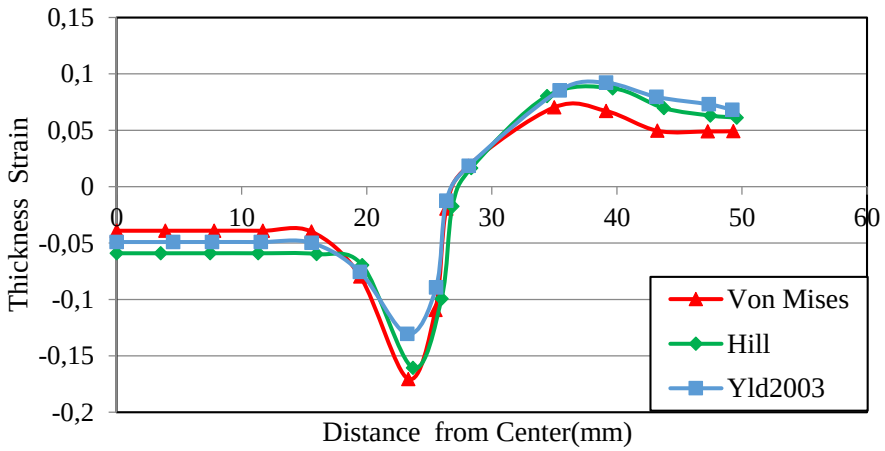

Figure 6.27 Thickness strain distribution for 200 mm/s punch velocity of AZ31 material for different yield criteria in 150°C temperature

6.4.3. Square Punch

6.4.3.1. DKP6112 Material in Rolling Direction

For DKP6112 material at room temperature, the variations of thickness strain values with respect to the center of blank in rolling direction results for 200 mm/s punch velocity by using different yield criteria are given in *Figure 6.28*. In critical thinning region, Yld2003 criteria gives slightly lower thickness strains. For cup flange region,

Hill48 estimates greater thickening from the other criteria. Yld2003 and von Mises give similar results in cup flange region.

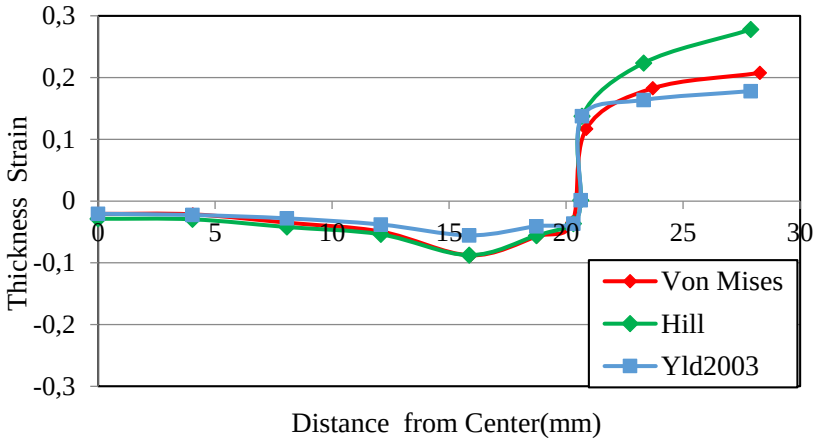

Figure 6.28 Thickness strain distribution for 200 mm/s punch velocity of DKP6112 material in rolling direction for different yield criteria in room temperature

6.4.3.2. DKP6112 Material in Diagonal Direction

For DKP6112 material at room temperature, thickness strain distribution according to the center of blank in diagonal direction results 200 mm/s case by using different yield criteria are given in *Figure 6.29.*

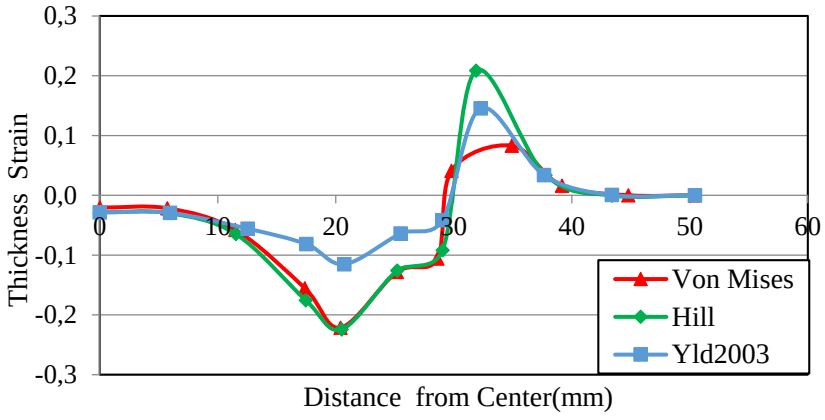

Figure 6.29 Thickness strain distribution for 200 mm/s punch velocity of DKP6112 material in diagonal direction for different yield criteria in room temperature

For critical thinning region, Yld2003 gives lower thickness strain values than the others. For maximum thickening region, anisotropic yield criteria Hill48 and Yld2003 estimate greater thickness strains.

6.4.3.3. AZ31 Material in Rolling Direction

For AZ31 material at room temperature, thickness strain distribution according to the center of blank in rolling direction results 200 mm/s case using different yield criteria are given in *Figure 6.30*. For the region below the punch, Yld2003 gives slightly lower thickness strains. For cup flange region, Hill48 estimates greater than the other model. For the same region, Yld2003 estimates the lowest thickness strain values.

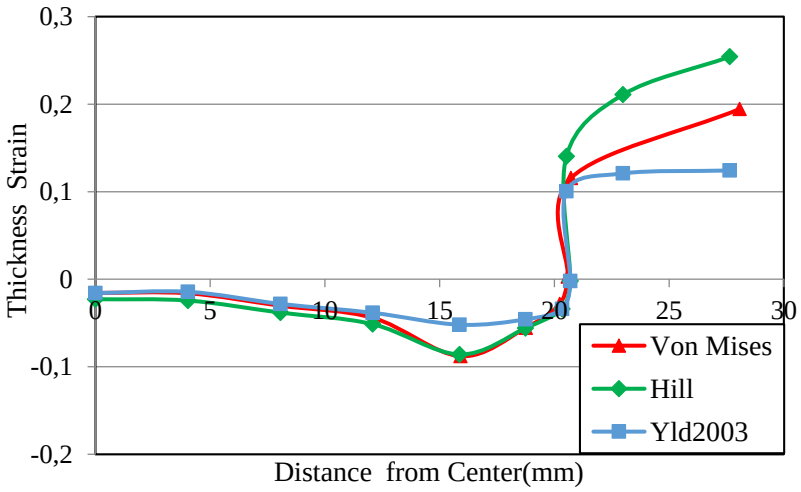

Figure 6.30 Thickness strain distribution for 200 mm/s punch velocity of AZ31 material in rolling direction for different yield criteria in room temperature

For AZ31 material at 150°C temperature, thickness strain vs. distance from center of the blank in rolling direction results for quasi-static case with different yield criteria is given in *Figure 6.31*. For cup flange and critical thinning region, Yld2003 yield

criterion estimates lower thickness strain values. Hill48 and von Mises yield criteria give close results for all regions in general.

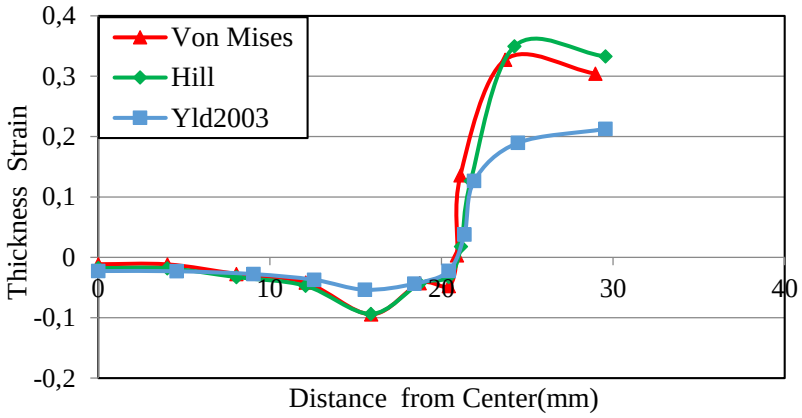

Figure 6.31 Thickness strain distribution for quasi-static case of AZ31 material in rolling direction for different yield criteria in 150°C temperature

For AZ31 material at 150°C temperature, the variations of thickness strain values with respect to the center of blank for 200 mm/s punch velocity by using different yield criteria are given in *Figure 6.32*.

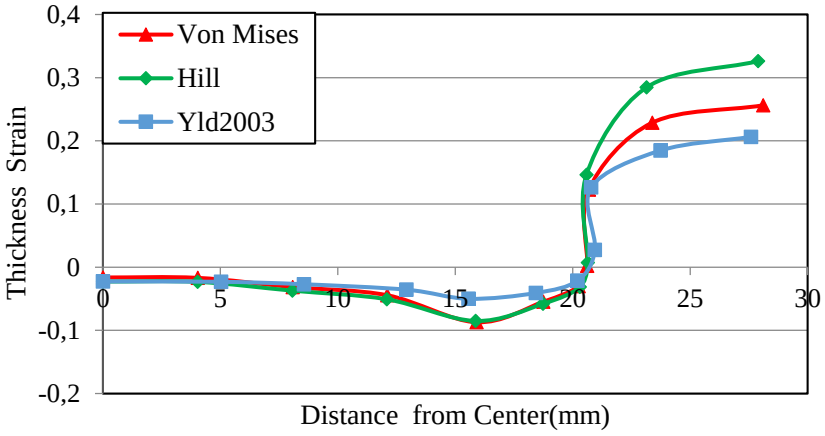

Figure 6.32 Thickness strain distribution for 200 mm/s punch velocity of AZ31 material in rolling direction for different yield criteria in 150°C temperature

In critical thinning and cup flange region, Yld2003 gives thickness strain values lower than the others. Hill48 yield criterion estimates thickening the greatest for cup flange region.

6.4.3.4. AZ31 Material in Diagonal Direction

For AZ31 material in room temperature, the variations of thickness strain values with respect to the center of blank in diagonal direction results 200 mm/s, 150°C and 200 mm/s 150°C cases by using different yield criteria are given in *Figure 6.33*, *Figure 6.34* and *Figure 6.35*. For critical thinning section in the region below the punch, Yld2003 estimates significantly lower thickness strain values than the other criteria for all conditions. For 200 mm/s at room temperature and 200 mm/s 150°C conditions, Yld2003 gives lower thickness strains in maximum thickening region. For 150°C quasi-static case, all of the criteria gives similar result for maximum thickening region.

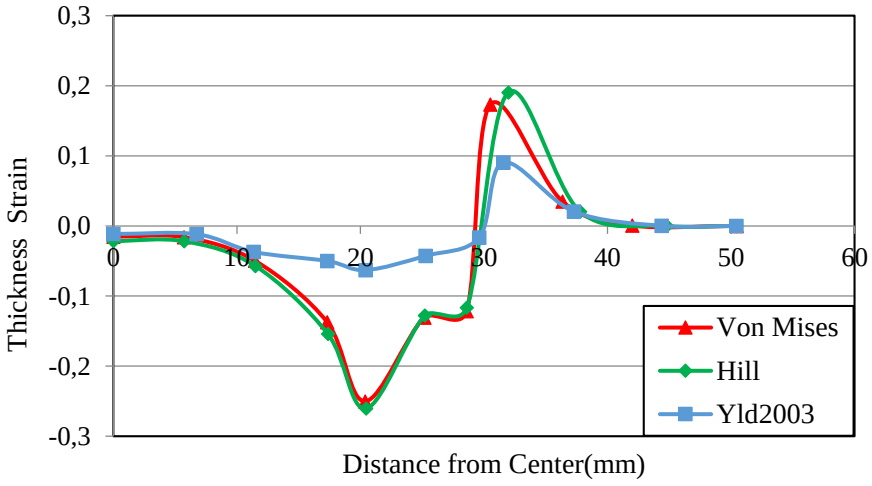

Figure 6.33 Thickness strain distribution for 200 mm/s punch velocity of AZ31 material in rolling direction for different yield criteria in room temperature

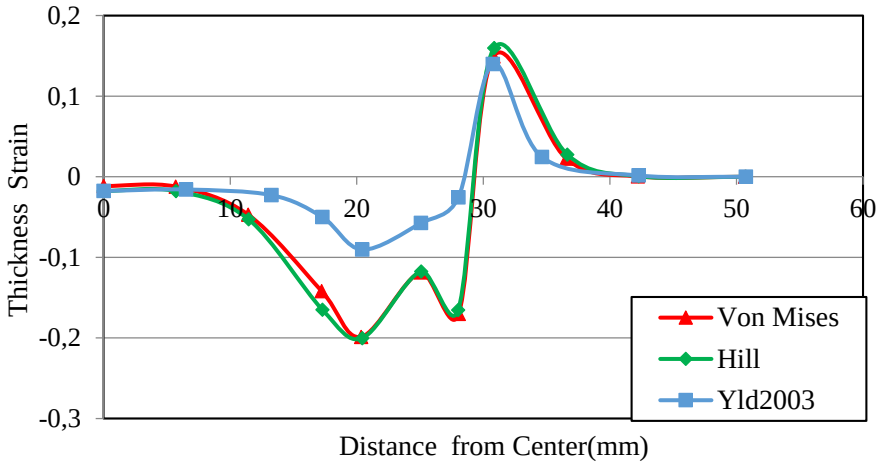

Figure 6.34 Thickness strain distribution for quasi-static case of AZ31 material in diagonal direction for different yield criteria in 150°C temperature

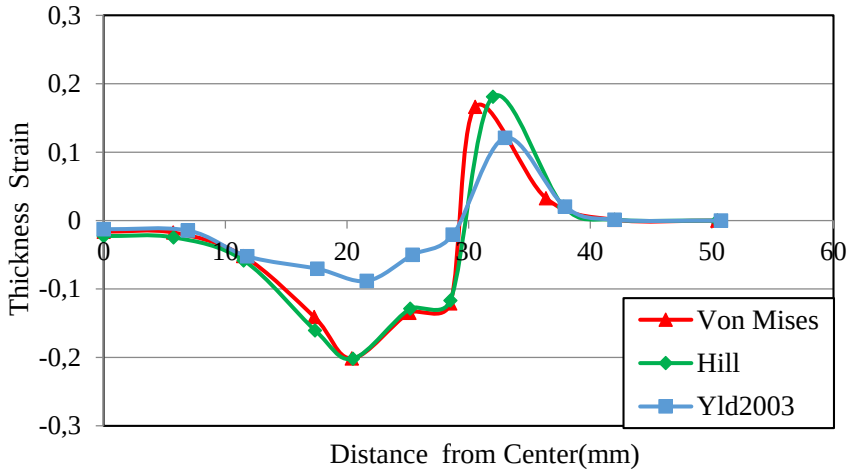

Figure 6.35 Thickness strain distribution for 200 mm/s punch velocity of AZ31 material in diagonal direction for different yield criteria in 150°C temperature

According to results, it can be concluded that YLD2003-8p yield criteria estimates thickness strain for the region below the punch lower than the other models since Von Mises and Hill48 criteria have approaches more conservative.

6.5. Forming Limit Diagram Analysis Results

6.5.1. DKP6112 Numerical Model Verification with Quasi-static Case

To verify the numerical model and to observe whether numerical simulations approximate the actual case accurately, analyses are performed for quasi-static case using DKP6112 material. Experimental and numerical results are compared in *Figure 6.36*.

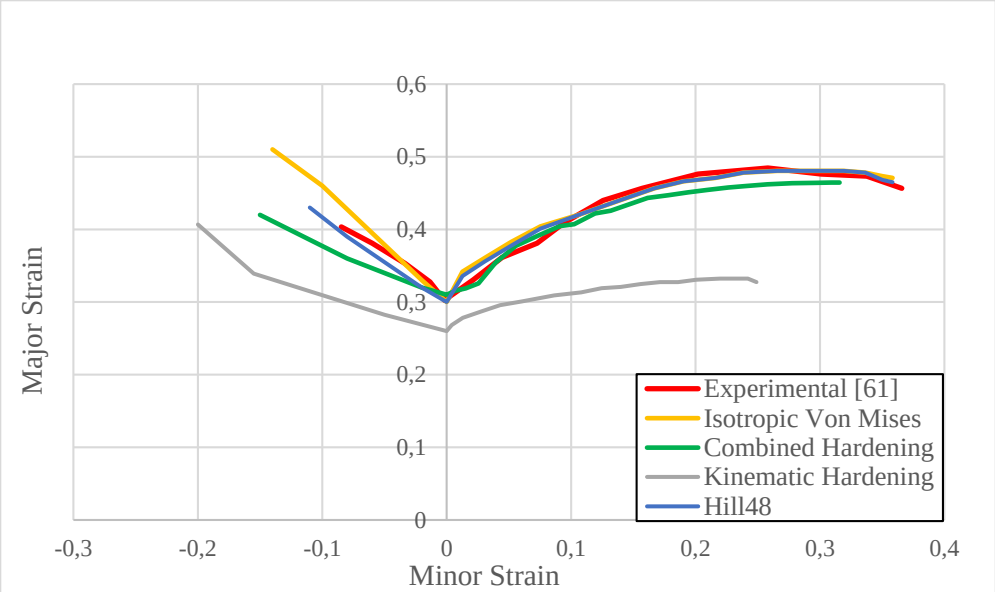

Figure 6.36 Experimental and numerical forming limit diagram of DKP6112 for quasi-static case and room temperature

From the comparison of experimental and numerical results, it can be observed that Hill48 yield criterion gives the closest results to experimental finding when $\varepsilon_1 > 0$. All of the other models predict FLD for DKP6112 quite well except von Mises yield criterion with kinematic hardening model when $\varepsilon_1 > 0$. For $\varepsilon_1 < 0$, isotropic Von-Mises model results in higher minor strain whereas von Mises yield criteria with combined hardening models predict lower values than the experiments. Von Mises

yield criterion with kinematic hardening deviates considerably. Hill48 has a good prediction for $\varepsilon_1 > 0$.

6.5.2. AZ31 Numerical Model Verification with 150°C Quasi-static Case

To verify the model for AZ31 material, the results of numerical model with different hardening models and yield criteria were compared with experimental results [60] for 150°C quasi-static case. Comparison of experimental and numerical results is given in *Figure 6.37*.

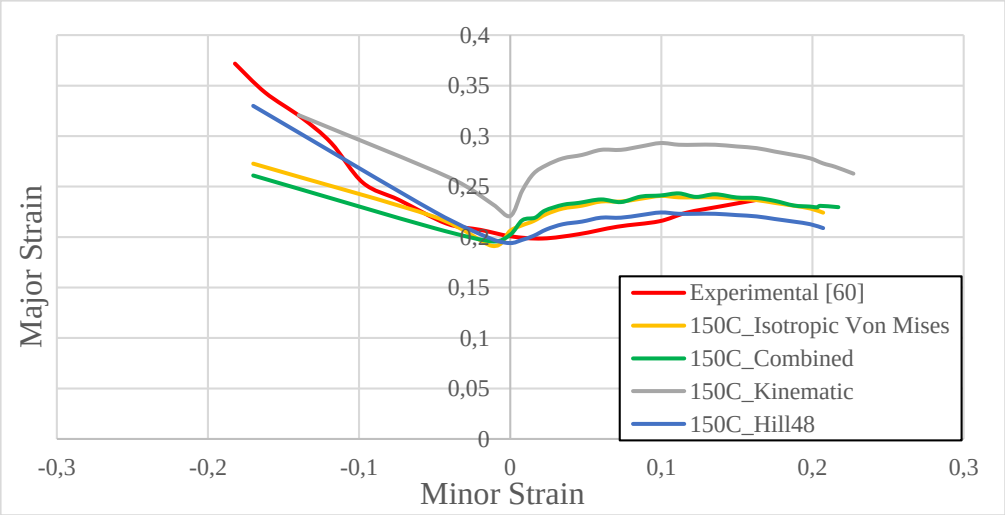

Figure 6.37 Experimental and numerical forming limit diagram of AZ31 for quasi-static case and 150°C temperature

Numerical simulation results give close estimates to the experimental results similar to DKP6112. Hill48 is the yield criterion that has closest results to the experimental findings. Isotropic and combined hardening models with von Mises yield criterion give higher values for $\varepsilon_1 > 0$ and lower values for $\varepsilon_1 < 0$ compared to experiments.

Results for von Mises with kinematic hardening model deviates significantly from experimental data.

6.5.3. Results for Different Strain Rate and Temperatures

6.5.3.1. DKP6112 Material

The same model which has been verified for quasi-static case was used for different punch velocities. Johnson-Cook constitutive model and Hill48 yield criterion were used for analysis of dynamic case. For DKP6112 material, to observe the effect of different punch velocities on forming limit diagram, numerical FLD for quasi-static and dynamic cases are compared in *Figure 6.38*.

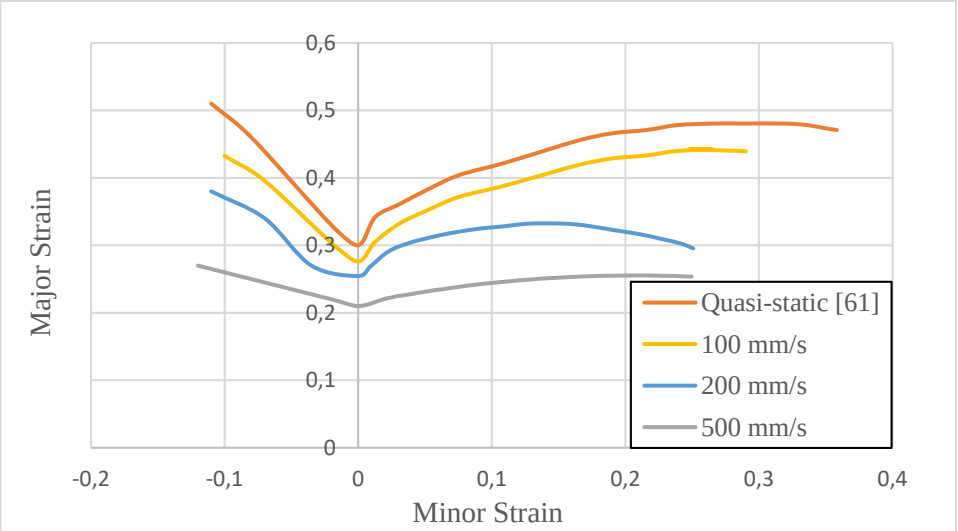

Figure 6.38 Comparison of numerical forming limit diagram of DKP6112 material for different punch velocity values in room temperature

It is observed that forming limit diagram shifts downwards and necking time is reduced with punch velocity increase. It can be commented that with punch velocity increase blank is more prone to fracture in relatively lower strain values.

6.5.3.2. AZ31 Material

According to results for AZ31 material given in *Figure 6.39*, it can be observed that with the increase of punch velocity, forming limit diagram shifts downwards and with the increase of temperature, forming limit diagram shifts upwards and necking time is increased.

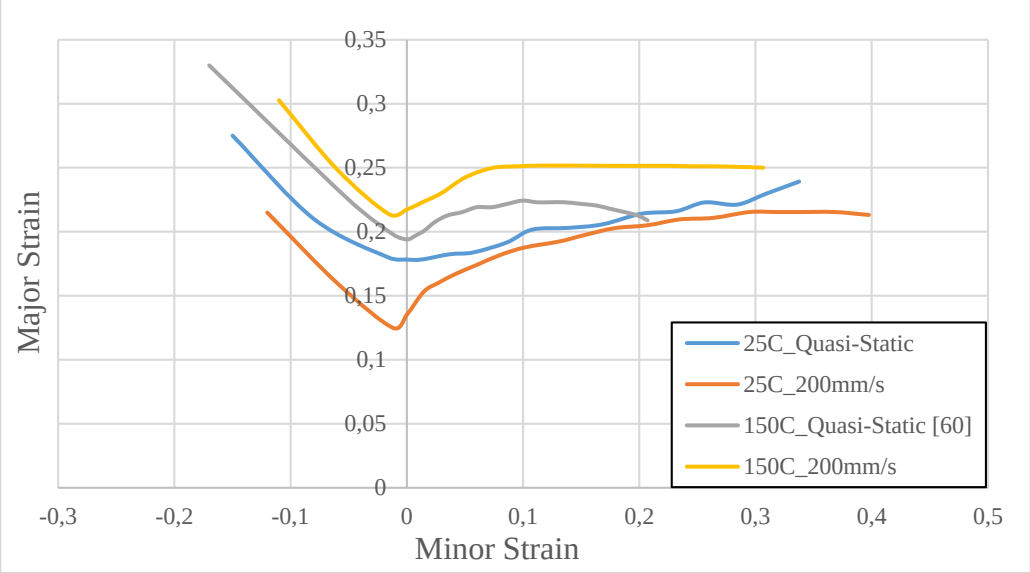

Figure 6.39 Comparison of numerical forming limit diagram of AZ31 material for different punch velocities and temperatures

It can be generally commented that increasing punch velocity has positive effect on minimum thicknesses, however it makes the blank being more prone to fracture due to decrease in ductility. In addition, greater punch forces are required for higher strain

rates. Increasing temperature decreases the possibility of fracture and it requires lower punch forces, however it has negative effect on minimum thicknesses.

6.6. Conclusion

In this study, the effects of punch velocity and temperature on thickness strain, punch force and forming behavior of DKP6112 steel and AZ31 aluminum-magnesium alloy materials of 1 mm thicknesses were investigated. For this purpose, hemispherical, cylindrical and square-shaped punches were used. Finite element model for all punch configurations were verified by the experimental results for quasi-static case with different yield criteria and hardening rules.

The followings were concluded from the study:

1. Thickness strain in the region prone to fracture decreases with strain rate increase and increases with the increase of temperature.
2. Punch forces are lower for elevated temperatures, however increasing strain rate increases required punch forces.
3. Thickness strain, distributions show that the effects of strain rate and temperature are dependent on die geometry. For hemispherical punch, the effect of strain rate and temperature are more pronounced. However, for cylindrical and square punch configurations the material flow is concentrated at the corner regions and closer results are observed at the other regions for different strain rate and temperatures. It can be stated that strain rate and temperature effects are more dominant for relatively smooth-shaped punch and die configurations where the material flow is relatively easier for all blank area.
4. The thickness strain distributions were found close to each other for different phenomenological models at low strain rate and temperatures. Hence, it is

observed that, in deep drawing operation, for low punch velocity values different models give close results.

5. For deep drawing process at high strain rates and elevated temperatures, it is convenient to prefer Johnson-Cook model due to its easy implementation.
6. Yld2003-8p gives most reliable results compared to Von-Mises and Hill yield criteria according to thickness strain distribution values.
7. According to the results of forming limit diagrams obtained numerically, FLDs shift downwards with increasing strain rate and shift upwards with increasing temperature. As a result, the blank is more sensitive to fracture when strain rate increases and temperature decreases.

6.7. Future Work

As a future work, necessary experimental work must be performed with given conditions in Chapter 5 to observe the validity and applicability of the assumptions about change of anisotropy coefficient with strain rate. Similarly, to verify the numerical forming limit diagrams from finite element simulations, Nakazima test can be performed for the given conditions and punch configurations. Friction coefficient is another concept that is included in future work. In this study, friction coefficient can be taken as the same for all strain rate and temperature values. For accurate modelling of friction condition, different friction models that include strain rate and temperature terms can be used and friction coefficient is calculated case-by-case.

REFERENCES

[1] Johnson, G. R., and Cook, W. H., 1983, "A Constitutive Model and Data for Metals Subjected to Large Strains, High Strain Rates and High Temperatures," Proc. 7th Int. Symp. Ballist., pp. 541–547.

[2] Zerilli, F. J., and Armstrong, R. W., 1988, "Dislocation Mechnics Based Analysis of Material Dynamics Behavior," Le J. Phys. Colloq., **49**(C3), pp. 529–534.

[3] Simulia, 2012, "Getting Started with Abaqus: Interactive Edition," p. 4.50-4.54.

[4] Cogun, F., 2015, "Comparison of Different Yield Criteria in Various Deep Drawn Cups," Int. J. Mater. Form., **10**(1), p. 85.

[5] Hill, R., 1948, "A Theory of the Yielding and Plastic Flow of Anisotropic Metals," Proc. R. Soc. London, **193**(1033), pp. 281–297.

[6] Comsa, D., and Banabic, D., 2008, "Plane-Stress Yield Criterion for Highly-Anisotropic Sheet Metals," *Numisheet 2008*, Interlaken, Switzerland, pp. 43–48.

[7] Aretz, H., 2005, "A Non-Quadratic Plane Stress Yield Function for Orthotropic Sheet Metals," J. Mater. Process. Technol., **168**(1), pp. 1–9.

[8] Dizaji, S. A., 2014, "An Investigation of Ductile Fracture Criteria for Sheet Metal Forming (PhD. Thesis)," Middle East Technical University, Ankara, Turkey.

[9] Ucan, M., 2011, "Effect of Constitutive Modeling in Sheet Metal Forming (MSc. Thesis)," Middle East Technical University, Ankara, Turkey.

[10] Baspinar, M., and Akkök, M., 2015, "Modeling and Simulation of Friction in Deep Drawing," J. Tribol., **138**(2), p. 021104.

[11] Panov, V., 2006, “Modelling of Behaviour of Metals at High Strain Rates (PhD. Thesis),” Cranfield University,Cranfield, United Kingdom.

[12] Smerd, R., Winkler, S., Salisbury, C., Worswick, M., Lloyd, D., and Finn, M., 2006, “High Strain Rate Tensile Testing of Automotive Aluminum Alloy Sheet,” Int. J. Impact Eng., **32**(1–4), pp. 541–560.

[13] Yoshida, F., Hamasaki, H., and Uemori, T., 2013, “A User-Friendly 3D Yield Function to Describe Anisotropy of Steel Sheets,” Int. J. Plast., **45**, pp. 119–139.

[14] Barlat, F., Brem, J. C., Yoon, J. W., Chung, K., Dick, R. E., Lege, D. J., Pourboghrat, F., Choi, S. H., and Chu, E., 2003, “Plane Stress Yield Function for Aluminum Alloy Sheets—part 1: Theory,” Int. J. Plast., **19**(9), pp. 1297–1319.

[15] Aretz, H., and Barlat, F., 2013, “New Convex Yield Functions for Orthotropic Metal Plasticity,” Int. J. Non. Linear. Mech., **51**, pp. 97–111.

[16] Yoon, J. H., Cazacu, O., Whan Yoon, J., and Dick, R. E., 2010, “Earing Predictions for Strongly Textured Aluminum Sheets,” Int. J. Mech. Sci., **52**(12), pp. 1563–1578.

[17] Plunkett, B., Cazacu, O., and Barlat, F., 2008, “Orthotropic Yield Criteria for Description of the Anisotropy in Tension and Compression of Sheet Metals,” Int. J. Plast., **24**(5), pp. 847–866.

[18] Yoon, J. W., Barlat, F., Dick, R. E., and Karabin, M. E., 2006, “Prediction of Six or Eight Ears in a Drawn Cup Based on a New Anisotropic Yield Function,” Int. J. Plast., **22**(1), pp. 174–193.

[19] Banabic, D., Aretz, H., Comsa, D. S., and Paraianu, L., 2005, “An Improved Analytical Description of Orthotropy in Metallic Sheets,” Int. J. Plast., **21**(3), pp. 493–512.

[20] Rule, W. K., and Jones, S. E., 1998, “A Revised Form for the Johnson-Cook Strength Model,” Int. J. Impact Eng., **21**(8), pp. 609–624.

[21] Couque, H., 2014, “The Use of the Direct Impact Hopkinson Pressure Bar Technique to Describe Thermally Activated and Viscous Regimes of Metallic Materials,” Philos. Trans. R. Soc., **372**(2023), p. 20130218.

[22] Tuazon, B. J., Bae, K. O., Lee, S. H., and Shin, H. S., 2014, “Integration of a New Data Acquisition/Processing Scheme in SHPB Test and Characterization of the Dynamic Material Properties of High-Strength Steels Using the Optional Form of Johnson-Cook Model,” J. Mech. Sci. Technol., **28**(9), pp. 3561–3568.

[23] Al Salahi, A. A., and Othman, R., 2016, “Constitutive Equations of Yield Stress Sensitivity to Strain Rate of Metals: A Comparative Study,” J. Eng., **2016**, pp. 1–7.

[24] Khan, A. S., and Baig, M., 2011, “Anisotropic Responses, Constitutive Modeling and the Effects of Strain-Rate and Temperature on the Formability of an Aluminum Alloy,” Int. J. Plast., **27**(4), pp. 522–538.

[25] Khan, A. S., and Liang, R., 1999, “Behaviors of Three BCC Metal over a Wide Range of Strain Rates and Temperatures: Experiments and Modeling,” Int. J. Plast., **15**(10), pp. 1089–1109.

[26] Verleysen, P., Peirs, J., Van Slycken, J., Faes, K., and Duchene, L., 2011, “Effect of Strain Rate on the Forming Behaviour of Sheet Metals,” J. Mater. Process. Technol., **211**(8), pp. 1457–1464.

[27] Khan, A. S., Baig, M., Choi, S. H., Yang, H. S., and Sun, X., 2012, “Quasi-Static and Dynamic Responses of Advanced High Strength Steels: Experiments and Modeling,” Int. J. Plast., **30**–**31**, pp. 1–17.

[28] Naka, T., Uemori, T., Hino, R., Kohzu, M., Higashi, K., and Yoshida, F., 2008, “Effects of Strain Rate, Temperature and Sheet Thickness on Yield Locus of AZ31 Magnesium Alloy Sheet,” J. Mater. Process. Technol., **201**(1–3), pp.

395–400.

[29] Huh, J., Huh, H., and Lee, C. S., 2013, “Effect of Strain Rate on Plastic Anisotropy of Advanced High Strength Steel Sheets,” Int. J. Plast., **44**, pp. 23–46.

[30] Roth, C. C., and Mohr, D., 2014, “Effect of Strain Rate on Ductile Fracture Initiation in Advanced High Strength Steel Sheets: Experiments and Modeling,” Int. J. Plast., **56**, pp. 19–44.

[31] Han, P., 1992, *Tensile Testing*, ASM International.

[32] Mamalis, A. G., Manolakos, D. E., and Baldoukas, A. K., 1997, “Simulation of Sheet Metal Forming Using Explicit Finite-Element Techniques: Effect of Material and Forming Characteristics Part 1. Deep-Drawing of Cylindrical Cups,” J. Mater. Process. Technol., **72**(1), pp. 48–60.

[33] Shim, H. B., and Yang, D. Y., 2016, “Elastic-Plastic Finite Element Analysis of Deep Drawing Processes by Membrane and Shell Elements,” J. Manuf. Sci. Eng., **1**(August 1997), pp. 1–9.

[34] Jung, D. W., 1998, “Study of Dynamic Explicit Analysis in Sheet Metal Forming Processes Using Faster Punch Velocity and Mass Scaling Scheme,” J. Mater. Eng. Perform., **7**(4), pp. 479–490.

[35] Naka, T., and Yoshida, F., 1999, “Deep Drawability of Type 5083 Aluminium-Magnesium Alloy Sheet under Various Conditions of Temperature and Forming Speed,” J. Mater. Process. Technol., **89**–**90**, pp. 19–23.

[36] Colgan, M., and Monaghan, J., 2003, “Deep Drawing Process: Analysis and Experiment,” J. Mater. Process. Technol., **132**(1–3), pp. 35–41.

[37] Seth, M., Vohnout, V. J., and Daehn, G. S., 2005, “Formability of Steel Sheet in High Velocity Impact,” J. Mater. Process. Technol., **168**(3), pp. 390–400.

[38] Lee, Y. S., Kwon, Y. N., Kang, S. H., Kim, S. W., and Lee, J. H., 2008,

"Forming Limit of AZ31 Alloy Sheet and Strain Rate on Warm Sheet Metal Forming," J. Mater. Process. Technol., **201**(1–3), pp. 431–435.

[39] F. Ayari E. Bayraktar, T. L., 2009, "Parametric Finite Element Analysis of Square Cup Deep Drawing," Arch. Comput. Mater. Sci. Surf. Eng., **1**(1), p. 6.

[40] Khan, A. S., Pandey, A., Gnäupel-Herold, T., and Mishra, R. K., 2011, "Mechanical Response and Texture Evolution of AZ31 Alloy at Large Strains for Different Strain Rates and Temperatures," Int. J. Plast., **27**(5), pp. 688–706.

[41] Khan, A. S., and Liu, H., 2012, "Variable Strain Rate Sensitivity in an Aluminum Alloy: Response and Constitutive Modeling," Int. J. Plast., **36**, pp. 1–14.

[42] Ma, W. Y., Wang, B. Y., Fu, L., Zhou, J., and Huang, M. D., 2015, "Effect of Friction Coefficient in Deep Drawing of AA6111 Sheet at Elevated Temperatures," Trans. Nonferrous Met. Soc. China (English Ed., **25**(7), pp. 2342–2351.

[43] Ghaffari Tari, D., Worswick, M. J., and Winkler, S., 2013, "Experimental Studies of Deep Drawing of AZ31B Magnesium Alloy Sheet under Various Thermal Conditions," J. Mater. Process. Technol., **213**(8), pp. 1337–1347.

[44] Huang, Y. M., Tsai, Y. W., and Li, C. L., 2008, "Analysis of Forming Limits in Metal Forming Processes," J. Mater. Process. Technol., **201**(1–3), pp. 385–389.

[45] Ozturk, F., and Lee, D., 2004, "Analysis of Forming Limits Using Ductile Fracture Criteria," J. Mater. Process. Technol., **147**(3), pp. 397–404.

[46] Karajibani, E., Hashemi, R., and Sedighi, M., 2017, "Forming Limit Diagram of Aluminum-Copper Two-Layer Sheets: Numerical Simulations and Experimental Verifications," Int. J. Adv. Manuf. Technol., **90**(9–12), pp. 2713–2722.

[47] Chalal, H., and Abed-Meraim, F., 2017, “Determination of Forming Limit Diagrams Based on Ductile Damage Models and Necking Criteria,” Lat. Am. J. Solids Struct., **14**(10), pp. 1872–1892.

[48] Lumelskyj, D., Rojek, J., and Tkocz, M., 2015, “Numerical Simulations of Nakazima Formability Tests With Prediction of Failure,” Rom. J. Tech. Sci. Appl. Mech., **60**(3), pp. 184–194.

[49] Khan, Akhtar S.; Huang, S., 1995, *Continuum Theory of Plasticity*, John Wiley & Sons.

[50] Lin, Y. C., and Chen, X. M., 2010, “A Combined Johnson-Cook and Zerilli-Armstrong Model for Hot Compressed Typical High-Strength Alloy Steel,” Comput. Mater. Sci., **49**(3), pp. 628–633.

[51] Slota, J., 2005, “Comparison of the Forming - Limit Diagram (Fld) Models for Drawing Quality (Dq) Steel Sheets,” Metalurgija, **44**, pp. 249–253.

[52] Wang, L., Chan, L. C., and Lee, T. C., 2008, “Formability Analysis of Magnesium Alloy Sheets at Elevated Temperatures With Experimental and Numerical Method,” J. Manuf. Sci. Eng., **130**(6), p. 061003.

[53] Bleck, W., Deng, Z., Papamantellos, K., and Gusek, C. O., 1998, “A Comparative Study of the Forming-Limit Diagram Models for Sheet Steels,” J. Mater. Process. Technol., **83**(1–3), pp. 223–230.

[54] Lumelskyj, D., Rojek, J., and Tkocz, M., 2018, “Detection of Strain Localization in Numerical Simulation of Sheet Metal Forming,” Arch. Civ. Mech. Eng., **18**(2), pp. 490–499.

[55] Zhang, C., Leotoing, L., Zhao, G., Guines, D., and Ragneau, E., 2011, “A Comparative Study of Different Necking Criteria for Numerical and Experimental Prediction of FLCs,” J. Mater. Eng. Perform., **20**(6), pp. 1036–1042.

[56] Lumelskyj, D., Rojek, J., Banabic, D., and Lazarescu, L., 2017, “Detection of Strain Localization in Nakazima Formability Test - Experimental Research and Numerical Simulation,” Procedia Eng., **183**, pp. 89–94.

[57] Kolasangiani, K., Shariati, M., and Farhangdoost, K., 2015, “Prediction of Forming Limit Curves (FLD , MSFLD and FLSD) and Necking Time for SS304L Sheet Using Finite Element Method and Ductile Article Info :,” J. Comput. Appl. Res. Mech. Eng., **4**(2), pp. 121–132.

[58] Petek, A., Pepelnjak, T., and Kuzman, K., 2005, “An Improved Method for Determining a Forming Limit Diagram in the Digital Environment,” J. Mech. Eng., **51**(6), pp. 330–345.

[59] Bonorchis, D., 2003, “Implementation of Material Models for High Strain Rate Applications as User-Subroutines in Abaqus/Explicit (MSc. Thesis),” University of Cape Town, South Africa.

[60] Zhang, K. F. Ã., Yin, D. L., and Wu, D. Z., 2006, “Formability of AZ31 Magnesium Alloy Sheets at Warm Working Conditions,” Int. J. Mach. Tools Manuf., **46**(11), pp. 1276–1280.